university of groningen

faculty of science and engineering

# Onset and Mode Selection of Faraday Waves in Glycerol–Water Mixtures

## Physics Lab: Research Project


Sam Bakker, s6379486

Tsjeard Bron, s6341098

Mihnea Marcu, s6341721

Leonardo Miranda, s6219128


12 June 2026


**Abstract**

The onset and mode selection of Faraday waves in vertically oscillated glycerol-water mixtures was investigated in this report. Fractions between 20 wt% and 80 wt% glycerol were oscillated with frequencies varying from 15 Hz to either 30 Hz or 50 Hz. The Faraday waves are expected to behave subharmonically or harmonically.

The Faraday waves were measured in a square container with a dotted grid below. The surface was filmed from above, after which surface reconstruction, via Free-Surface Synthetic Schlieren (FSSS), based on the displacement of the dots on the grid due to the refraction index of the solution was performed.

After analysing these results with a Fourier transform, the main objective was to experimentally confirm previously established theory around Faraday waves, encapsulated in four research questions.

After measuring, two questions regarding onset acceleration of Faraday waves were not definitively answered due to a systematic overestimation in experimental data. It can be cautiously concluded that the relative trend of the experimental results followed the theoretical trend for onset acceleration.

For the other two questions, the behaviour of Faraday waves was confirmed to be subharmonic and harmonic. The dispersion relation for gravity-capillary waves was confirmed for Faraday waves. A slope of $1.05 \pm 0.02$ was found between experimentally determined and wavenumbers predicted by the gravity-capillary wave equation, where a slope of 1 would be a perfect match between experiment and theory.

# Contents

# 1 Introduction

In 1831, a publication of Michael Faraday appeared in *Philosophical Transactions of the Royal Society*. In the original paper, Faraday was researching so-called Chladni patterns: patterns that sand grains form on a plate when the plate is vibrated by sound waves. In his experiment, he not only put grains on a vibrating plate, but also tried using fluids like water. He called the standing waves that formed "crispations", now known as Faraday waves. He even described the subharmonic behaviour of these patterns. The way in which these waves can be studied with fluid dynamics combined with the patterns that are formed makes this an excellent topic for both qualitative and quantitative research [1]. This report will mainly focus on the quantitative part.

## 1.1 Conceptual

This introduction is based on the research papers from Pedersen et al. [2], and Kumar and Tuckerman [3]. When a bath is oscillated vertically by a shaker, Faraday waves appear. As mentioned above, the waves generally exhibit subharmonic behaviour if the driving acceleration is below some threshold. Harmonic behaviour can be observed if the driving acceleration is higher. This combined leads to the predicted angular frequencies with which the liquid oscillates [2] [3]:

$$\omega_0 = \frac{n}{2}\omega_d, \tag{1}$$

where $\omega_0$ is the response angular frequency of the liquid, $\omega_d$ is the angular driving frequency and $n$ is an integer. Odd $n$ means subharmonic behaviour and even $n$ means harmonic behaviour by definition.

The waves are standing waves and are, by definition, caused only by the vertical motion of the bath. Experimenters would ideally work with an infinitely large bath, as this prevents any external phenomena from forming waves.

The stability of the fluid is characterised by "instability tongues". These tongues define the acceleration at which the fluid becomes unstable and starts to oscillate. An instability tongue is made for one single driving frequency. See page 59 of Kumar and Tuckerman [3] for precise figures of these instability tongues. The minimum acceleration that causes the instability in the fluid at a given wavelength is called the critical acceleration $a_c$. The properties of the liquid, such as surface tension and viscosity, influence the instability tongues.

There is one wavelength for which the critical acceleration is the lowest out of all wavelengths. This will be referred to as the onset acceleration $a_z$. Unlike $a_c$, $a_z$ can be measured without analysing the wavelengths of appearing waves. $a_z$ is equal to the lowest driving acceleration $a_d$ at which instability is observed. The wavenumber that corresponds to $a_z$ is the resonant wavenumber, as it becomes unstable most easily.

A property of Faraday waves is that the wavelength is not a direct input parameter, but a reaction to the driving force. The reason for this is that the driving force only indirectly influences the liquid in the bath. The range of wavelengths that appear in waves is characterised precisely by the mentioned instability tongues. The way Faraday waves work is that some possible wavelength of a Faraday wave can be unstable *for a given driving frequency and driving acceleration*.

## 1.2 Research questions

With the conceptual introduction out of the way, the research questions should be posed. Important parts of the theory will be verified. Note that some research questions will be understood more easily after reading the theory. An attempt will be made to answer the following research questions in this report:

1. Do vertically oscillated glycerol-water solutions exhibit subharmonic and harmonic behaviour?
2. How does viscosity affect the onset acceleration?
3. How does driving frequency affect the onset acceleration?
4. How well do measured wavenumbers follow the gravity-capillary dispersion relation when rectangular modes are taken into account?

The hypothesis for the first question is that both subharmonic and harmonic behaviour will be observed [2] [3]. This is equivalent to expecting Equation (1). Instability tongues show that the first subharmonic frequency is most unstable, which is why it is expected that every next $n$ will give an $\omega_z$ that is harder to observe [3].

The hypothesis for the next two research questions can be summarised with the Mathieu equation (Equation (3)). The behaviour of infinitesimal Faraday waves is governed by this equation, and the hypothesis is that it can predict instability [4]. The prediction is that the onset acceleration increases with viscosity according to the relation, since onset acceleration increases with the damping factor (Equation (13)) and the damping factor increases with viscosity (Equation (8)). The expectation is that the approximation for the damping factor is close to the real value, as relatively low damping will be used in this experiment [5].

There is not a similar relation between onset acceleration and driving frequency, as this relation does not have a closed form. A potential predicted relationship between onset acceleration and driving frequency can be found in Figure 2.

The hypothesis for the final research question is that the dispersion relation is closely followed by the waves, when corrected for rectangular modes. The correction is of the nature of calculating the allowed wavenumbers close to the resonant wavenumber. The expectation of a close relation is based on previous findings in literature [2].

The way Faraday waves were measured involved a rectangular bath containing a glycerol-water mixture. Measurements were taken by vertically oscillating a plate, and placing the bath on this plate. Under the container, a dotted grid was placed. Above the container, a camera filmed when performing measurements. Data could be extracted with FSSS surface reconstruction Section B.5, which utilised the displacement of the dots due to the other refractive index of water. A Fourier transform of the points over time was subsequently able to extract necessary data. The driving acceleration was measured using an accelerometer placed on the plate.

# 2 Theory

## 2.1 Dispersion relation

The relation of natural angular frequency with the wavenumber of a specific wave is given by the dispersion relation [2], [3]:

$$\omega_0^2 = \left(gk + \frac{\sigma}{\rho}k^3\right)\tanh(kh), \tag{2}$$

with $\omega_0$ the natural angular frequency of the wave, $g$ the gravitational constant, $k$ the wavenumber of a given wave, $\sigma$ the surface tension of the liquid, $\rho$ the density of the fluid and $h$ the depth of the bath.

In this experiment, it was found that the hyperbolic tangent cannot be approximated or neglected with the values in this experiment. This means the inverse relation (finding $k$ for given $\omega_0$) does not have a closed form and should be numerically approximated. See Section C for a straightforward way to do this.

Faraday waves do not have to behave exclusively in a subharmonic manner. From the equations governing fluids, a set of equations specifically for Faraday waves can be derived, which Kumar and Tuckerman [3] called the Full Hydrodynamic System. It turns out that these equations constitute so called "resonance tongues", as mentioned in the introduction. These can be obtained by plotting the stability boundary for critical acceleration $a_c$ against the wavenumber $k$.

## 2.2 Mathieu equation

A computational model was built to approximate the behaviour of Faraday waves. In this model, the Mathieu equation was used [4]:

$$\frac{d^2\zeta}{dt^2} + 2\gamma\frac{d\zeta}{dt} + \omega_0^2\left(1 - F\cos(\omega_d t)\right)\zeta = 0, \tag{3}$$

with $\zeta$ the displacement, $\gamma$ the damping coefficient, $\omega_0$ the angular frequency of waves, $F$ the dimensionless amplitude of the driving force, $\omega_d$ the angular frequency of the driving force and $t$ the time. It is important to note that this equation only holds for infinitesimal waves. The infinitesimal wave approximation works for predicting instability, but it cannot predict the final amplitude of waves. It predicts that waves will grow infinitely large, which is incorrect. Non-linear effects have to be taken into account for a more complete model (non-linear would mean a damping term proportional to for example $\zeta^3$) [4].

The dimensionless forcing term should be calculated. To figure out what it is exactly, we need the dispersion relation. The term that multiplies $\zeta$ is the time dependent angular frequency squared, which is influenced by the driving force. To calculate it, use that the effective gravity is given by:

$$g_{eff} = g - a_d\cos(\omega_d t), \tag{4}$$

with $a_d$ the amplitude of driving acceleration. If we substitute effective gravity for gravity into the dispersion relation, we get:

$$\omega^2(t) = ((g - a_d\cos(\omega_d t))k + \frac{\sigma}{\rho}k^3)\tanh(kh) = \omega_0^2 - a_d k\tanh(kh)\cos(\omega_d t) \tag{5}$$

$$F = \frac{\Gamma_d g k}{\omega_0^2}\tanh(kh), \tag{6}$$

with $\omega_0$ given in Equation (2), and where the non-dimensional acceleration

$$\Gamma_d = \frac{a_d}{g} \tag{7}$$

was introduced. Every time $\Gamma$ is used instead of $a$, the subscripts can be matched to see which quantity is discussed.

The only constant left to calculate in the Mathieu equation (Equation (3)) is $\gamma$. There are multiple sources of damping in Faraday waves. The model was built with bulk dissipation, which is related to the viscosity of the fluid, and friction with the bottom of the container ([4]):

$$\gamma = \nu k^2 \left(2 + \frac{\coth(2kh)}{\sinh(2kh)}\right) + \sqrt{\frac{k\nu\sqrt{gh}}{8}} \frac{2k}{\sinh(2kh)}, \tag{8}$$

with $\nu$ the kinematic viscosity, $h$ the container depth, and $g$ the gravitational constant. Meniscus damping and wall damping are not taken into account, as these are difficult to estimate and meniscus damping depends on microscopic properties of the container. $\gamma$ is therefore underestimated, which should be taken into account when interpreting the results.

## 2.3 Computational model

A computational model was built to both understand Faraday waves better, as well as find relations between physical quantities to answer the research questions. A mathematical branch studying stability was introduced to properly find unstable regions for Faraday waves. All necessary knowledge is introduced in Section A. The goal was to produce the following results with the computational model: reproduce resonance tongues as in [3], onset acceleration as a function of driving frequency, onset acceleration as a function of viscosity of the fluid, and an indication of how close the the subharmonic frequency approximation is according to the model.

As mentioned in Section A, the eigenvalues of the monodromy matrix can be used to separate stability from instability. Using this property, a root finding method can be used to find the boundary values of stability. The following graph was obtained for $f_d = 20$ Hz (Figure 1):

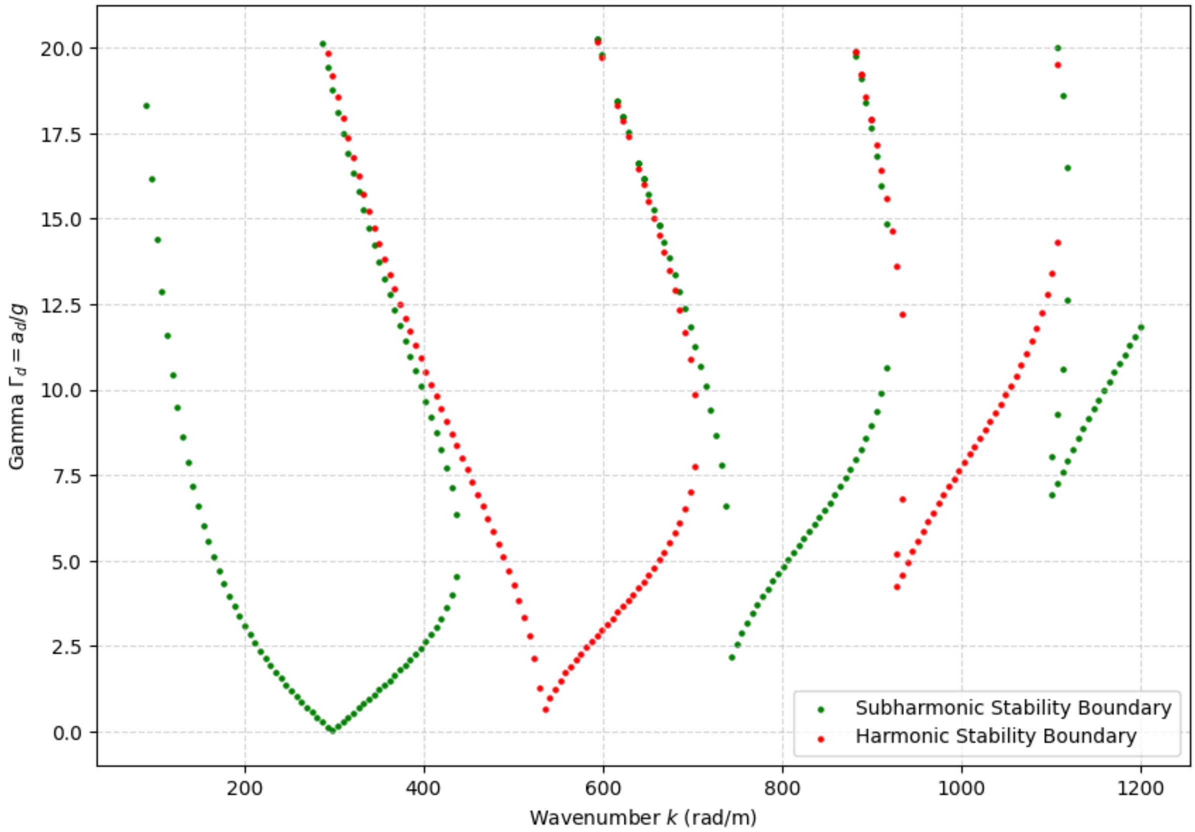


Figure 1: Stability boundary for Faraday waves of $\Gamma_d$ versus $k$ performed by numerically approximating eigenvalues of the monodromy matrix. Green indicates boundary values of a subharmonic tongue and red indicates boundary values of a harmonic tongue. Constants used in the model were: $g = 9.81$ m/s$^2$, $\sigma = 7.2 \times 10^{-2}$ N/m, $\rho = 1.0 \times 10^3$ kg/m$^3$, $\nu = 1.0 \times 10^{-6}$ m$^2$/s, $f_d = 20$ Hz, $h = 5.0 \times 10^{-3}$ m.

The way to interpret Figure 1 is that, given some acceleration and some wavenumber, instability is indicated if the point falls inside of one of the tongues (view one colour of points as "enclosing" a specific region). If the point falls in the first subharmonic tongue, a wave with the given wavenumber oscillates at half the driving frequency. A wave in the first harmonic tongue oscillates at the driving frequency, and a wave in the second subharmonic tongue oscillates at one and a half times the driving frequency [3].

This once again shows that Equation (2) can only relate natural frequency and wavenumber. The oscillation of the bath forces the waves to oscillate at a frequency that is different from their natural frequency. A consequence of this is that only subharmonic and harmonic frequencies should be observed in the experiment [3].

The minimum acceleration on the boundary of the tongue appears at $k = 270$ rad/m. This (standardised) acceleration is precisely the onset gamma $\Gamma_z$. If this is plugged into the dispersion relation (Equation (2)) and angular frequency is converted to frequency, a resonant frequency of $f_{res} = 10.1$ Hz is found, which is almost exactly half the driving frequency. Subharmonic resonance is intuitively expected to occur at a wavenumber corresponding to a natural frequency close to half the driving frequency, so this result was expected (as you can see in Figure 4, this is not an exact relationship).

An analytical solution for the relationship between onset acceleration and driving frequency does not exist, an approximation was made on page 255 of Luongo et al. [6]. The lowest instability boundary gives, when substituted:

$$2\frac{\gamma}{\omega_0} = \frac{1}{2}F \tag{9}$$

$$\Gamma_c = \frac{4\gamma\omega_0}{gk\tanh(kh)}, \tag{10}$$

where $\gamma$ is given in Equation (8), $F$ is given in Equation (6) and natural angular frequency can be approximated as $\omega_0 = \frac{1}{2}\omega_d$. The value for $k$ that corresponds to $\omega_0$ can be found by finding the inverse of the dispersion relation. A recommended way for doing this is using root finding with a program (Section C).

The onset acceleration found by the analytical approximation can be compared to the onset acceleration found by the numerical/computational method. Doing this, the following graph was obtained (Figure 2):

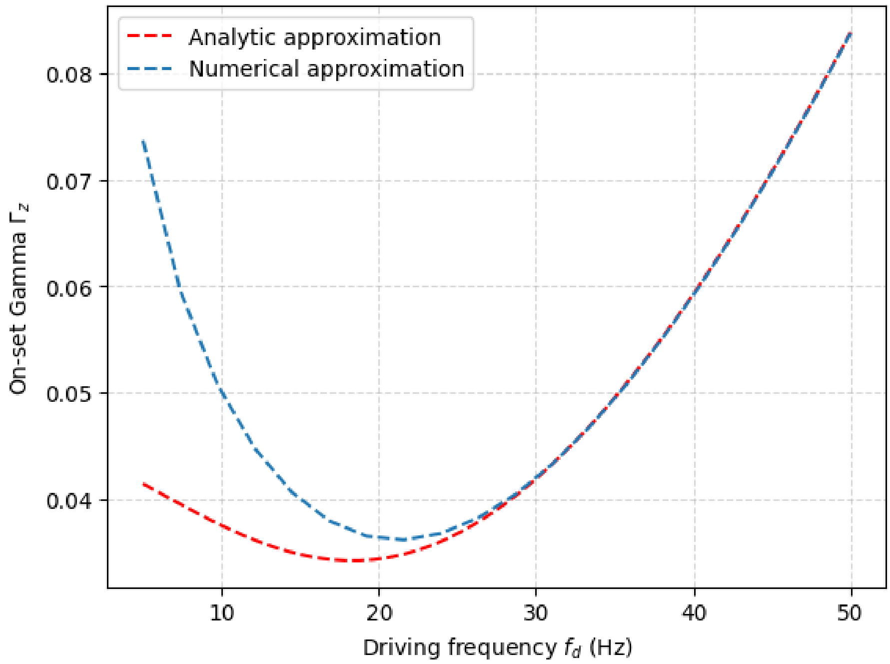


Figure 2: Onset gamma factor plotted against driving frequency with a comparison of the analytic and the numerical model with the constants: $g = 9.81$ m/s$^2$, $\sigma = 7.2 \times 10^{-2}$ N/m, $\rho = 1.0 \times 10^3$ kg/m$^3$, $\nu = 1.0 \times 10^{-6}$ m$^2$/s, $h = 5.0 \times 10^{-3}$ m.

The viscosity can be varied in exactly the same way, which yields the graph (Figure 3):

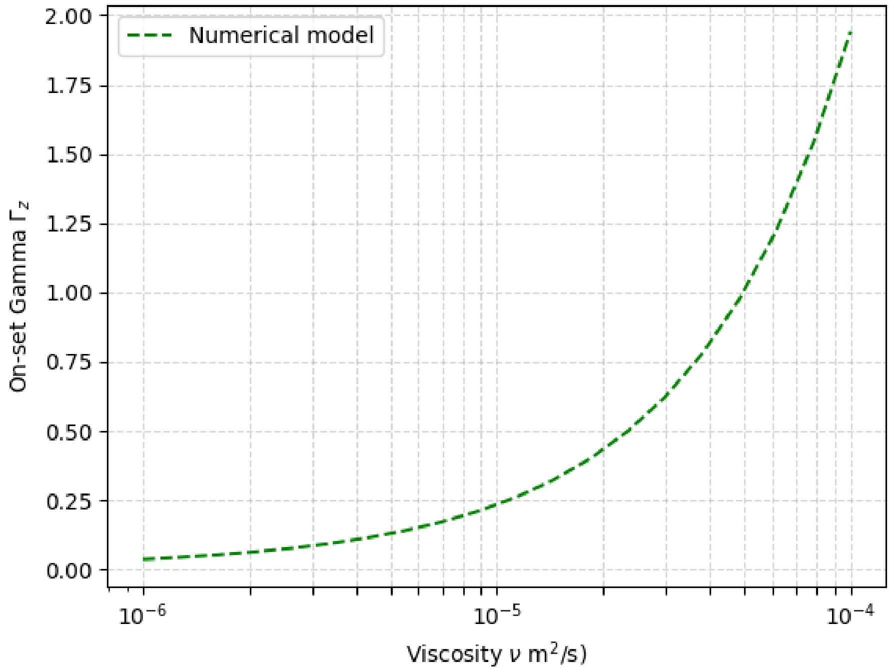


Figure 3: Onset Gamma factor plotted against viscosity on log-scale with constants: $g$ = 9.81 m/s$^2$, $\sigma$ = 7.2 × 10$^{-2}$ N/m, $\rho$ = 1.0 × 10$^3$ kg/m$^3$, $f_d$ = 20 Hz, $h$ = 5.0 × 10$^{-3}$ m.

With the same computational model, the frequency corresponding to this minimum acceleration $f_{res}$ can be found as a function of the driving frequency, see Figure 4:

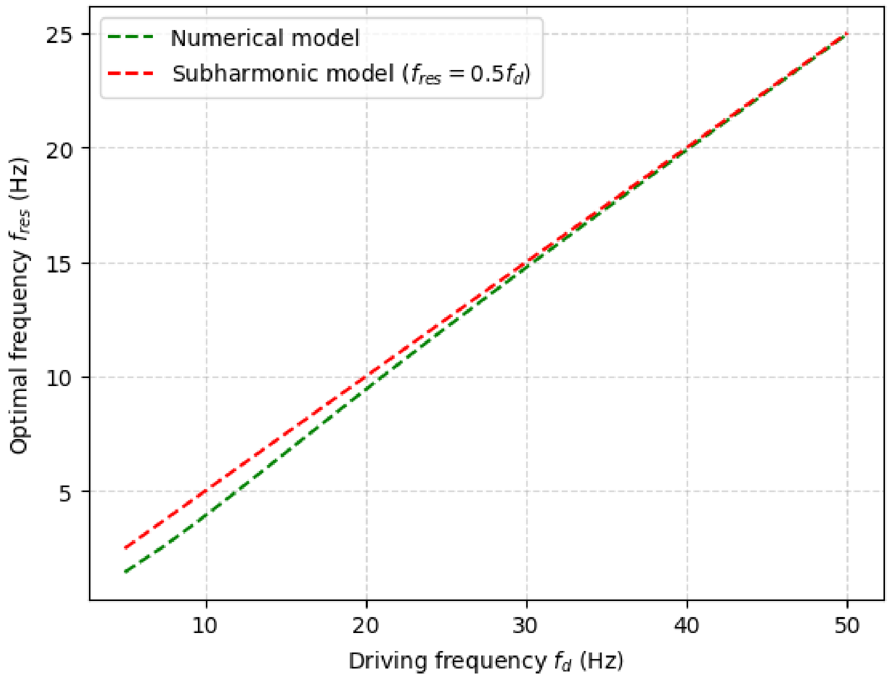


Figure 4: Plot of resonant frequency versus driving frequency, and the expected resonant frequency versus driving frequency with constants: $g$ = 9.81 m/s$^2$, $\sigma$ = 7.2 × 10$^{-2}$ N/m, $\rho$ = 1.0 × 10$^3$ kg/m$^3$, $\nu$ = 1.0 × 10$^{-6}$ m$^2$/s, $h$ = 5.0 × 10$^{-3}$ m.

The subharmonic approximation is close to the computational model and gives another justification for the hypothesis of the first research question.

An important disclaimer is that these numerical models were not used in the analysis of data in the end. Although the computational model has high precision, the cost of computational power is high. The model is therefore reserved to merely this theoretical section, and could be used in future research papers.

## 2.4 Rectangular modes

A caveat in the method used to approximate the onset acceleration is that a continuous range of possible wavenumbers was assumed, even though only specific wavelengths have a multiple that "fits" inside of the bath (so an infinite bath would not have this problem). Resonance will only occur when this condition is met, so a better approximation would only use discrete wavenumbers. The formula for "allowed" wavenumbers in a rectangular geometry is [2]:

$$\begin{aligned} k_{x,n} &= \frac{n\pi}{L_x} \\ k_{y,m} &= \frac{m\pi}{L_y} \end{aligned} \tag{11}$$

with $k_{x,n}$ and $k_{y,m}$ the wavenumbers for the x- and y-direction, $n$ and $m$ integers, and $L_x$ and $L_y$ the length of the bath in the x- and y-direction.

The wavenumbers that should be tested for instability in case of the waves in the rectangular mode are [2]:

$$k_{mn} = \sqrt{k_{x,n}^2 + k_{y,m}^2} = \pi\sqrt{\left(\frac{n}{L_x}\right)^2 + \left(\frac{m}{L_y}\right)^2}, \tag{12}$$

with $m, n \in \mathbb{N}_0$ and $(m, n) \neq (0, 0)$.

Finding critical acceleration for a finite rectangular bath is relatively straightforward, as a computational model can loop over the values for $k_{x,n}$ and $k_{y,m}$ to find the one with the lowest critical acceleration. Because a natural frequency close to the subharmonic frequency may not be allowed, a detuning term has to be added to the onset acceleration [5]:

$$\Gamma_c = \frac{2\omega_0\sqrt{(2\gamma)^2 + (\omega_d - 2\omega_0)^2}}{gk\tanh(kh)}. \tag{13}$$

A surface with wavenumbers $k_x$ and $k_y$ and the condition that there is no vertical displacement at the walls of the container, can be described as [2]:

$$\zeta(\mathbf{x}, t) = \zeta(t)\sin(k_x x)\sin(k_y y), \tag{14}$$

with $\zeta(\mathbf{x}, t)$ the height at given position with $\mathbf{x} = (x, y)$, and $\zeta(t)$ the amplitude of the height at a given time. As indicated before, Equation (3) predicts that waves will grow infinitely large and therefore $\zeta(t)$ cannot be found with this equation.

For visualization of Equation (14), the case of a very simple square box with only one resonant wavenumber was plotted in Figure 5:

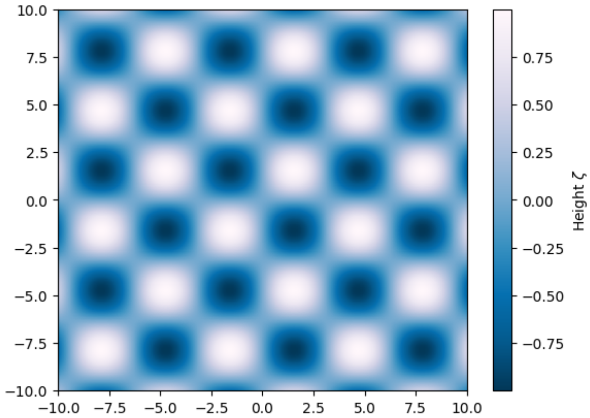


Figure 5: Colour map of a simple square box with wavenumbers $k_x = 1$ and $k_y = 1$.

# 3 Methods

As a preface, the experimental setup that was used for this research project was adapted from the setup designed by Pedersen et al. [2], being proposed as an undergraduate level fluid dynamics experiment.

## 3.1 Generating Faraday waves

First, a PASCO SF-9324 Mechanical Wave Driver is used in order to generate the vertical vibrations needed to generate the Faraday waves. This has to be paired together with the IPC-4885-W Signal Generator & Amplifier.

The SF-9324 Mechanical Wave Driver manual warns that only currents up to 1 A should be provided, such that, a Voltcraft VC830 Multimeter has to be connected in series, in order to monitor the current's intensity at all times. Although the multimeter cannot reliably show any values above 200 mA, we noticed that the current intensity does not reach that threshold for most of the frequency-amplitude pairings that were tested.

In order to achieve a working Faraday waves setup, a plate upon which the fluid bath could rest is required. This posed a few problems at first as the ones that were readily available in the lab seemed to each have different shortcomings, such as being too unstable once mounted or not being a good fit for the wave generator altogether. Fortunately enough, a different research team 14 had already solved this problem for their own experiment, having 3D printed a plate that fit perfectly into the wave driver. The plate was then kindly offered to us.

The final component needed to complete the functional Faraday waves setup is the bath. Initially, a circular Petri dish was used as the bath. However, it was quickly abandoned for multiple reasons such as the smaller surface area, noticeable disturbances caused by the lighting such as light caustics or concentrated bright spots on the fluid's surface, and complicated mathematics. All of these effects and issues were greatly reduced by using a square shaped, 10 mm × 10 mm, polystyrene container instead.

## 3.2 Recording Faraday waves

Measuring the Faraday waves was an experimentally challenging process. A typical measurement run consisted of recording the oscillating bath, while logging real time values of the envelope acceleration using an accelerometer chip.

The recordings of the waves allowed for a special surface reconstruction technique to be used. This method greatly relies on the lensing effect caused by disturbances on the surface of a transparent fluid. This is why, in order to be able to quantitatively describe the fluid's surface, an opaque dotted grid was placed underneath the transparent fluid container. This made it so that the dots would either change size or be displaced from the viewpoint of the camera, depending on the way that the light rays were refracted by the fluids surface. These distortions of the dotted grid were then analysed by a Python script. After giving the script enough information about the system, it was able to reconstruct the surface of the fluid, while also extracting the frequency and amplitude of the oscillations.

In order to protect the dotted grid from potential spillage, a 2 mm thick acrylic plate was placed above it, separating it from the bath. This addition affected the optics, as the extra transparent layer meant that the light rays would refract even more. This distortion was accounted for in the script.

The dotted grid that was used had a separation of 1 mm between dots, ensuring that they would be easily distinguishable in the recordings, while still being minute enough to provide great detail in the surface reconstruction.

Every video was recorded using the same camera and the same settings. The camera that was used was an iPhone 16's 26 mm back camera. The videos were taken from a top-down perspective, from a constant height of approximately 12.5 cm. More importantly, the recordings were taken in 240 Hz slow motion, at a resolution of $1920 \times 1080$ pixels. The range of driving frequencies used throughout the experiment was $15 - 50$ Hz. This implies that even for higher frequencies, 5 video frames were allocated per oscillation. This was more than enough to observe the motion in a detailed manner.

Levelling the plate was also done prior to most measurements in order to ensure the mass of the fluid was evenly distributed and that the motion of the wave driver was constrained to the $z$-axis as much as possible.

Another important addition to the setup was the 3D Scientific Optical Lamp, also mounted above the bath, at an angle between 30° and 40°. Once again, providing more visibility and depth to the recordings. In order to account for the increased amount of light reflecting off the fluid's surface, the shutter speed of the camera was set to $1/4000$ s, while the white balance was set to 3200 K.

The camera, along with the lamp, were fixed in place using stands, rods, clamps and connectors. These were assembled together and kept mostly unchanged throughout the experiment.

## 3.3 Logging $\Gamma$ values

As stated before, measurements were taken in a hybrid manner, by matching the aforementioned recordings with data from an Adafruit ADXL345 accelerometer that was mounted onto the plate using double sided tape. In order for the accelerometer to function, it had to be connected to an Arduino UNO R4 WIFI that ran a program that displayed the data of the accelerometer in real time, measuring the $\Gamma$ acceleration ratio alongside a number of other useful quantities. Most importantly, this chip has a sampling rate of 3200 Hz, more than ten times value of the highest measured driving frequency, providing great resolution.

The script also gave the option to log the $\Gamma$ values with respect to absolute time and export the data as a .CSV file. This made it possible to match the $\Gamma$ with the recorded oscillations, which is of great use for answering the second research question regarding the onset acceleration.

Prior to using the accelerometer, a different method for measuring the acceleration of the bath, adapted from Pedersen et al. [2], was attempted. It was expected that the bath's vertical vibrating motion could be derived by pointing a laser at the plate at an extremely shallow angle of approximately 10°. As a result, the laser point would also start oscillating horizontally, with the motion being recorded using the aforementioned top-down pointing camera. The oscillatory motions would then be related through the angle, which in turn would be determined through experiment. Unfortunately, once attempted, the horizontal motion of the laser was indistinguishable as the displacement of the point appeared to be smaller than the beam's radius, meaning that this method had to be abandoned. Taking everything into account, a laser with a small enough beam radius could be used to find the acceleration of the vibrating, making the accelerometer obsolete and simplifying the setup.

## 3.4 Fluid solutions

Two fluids were used for the entirety of the experiment, those being distilled water and glycerol. Faraday waves were measured for fluids of varying viscosity by making solutions consisting of 20%, 30%, 40%, 50%, 70% and 80% glycerol by mass. Glycerol has a higher viscosity than water, whilst being miscible in water, meaning it can be fully dissolved. The mass of the solutions varied slightly between experiments, but was always in the range of 60-70 g, to ensure that the fluid in the container was deep enough. Mass was not directly used in the computations, but was instead used as a way to calculate the fluid's depth, using other known quantities such as the volume of the container. Also, since the amplitude and frequency were measured directly, a varying mass should not be problematic.

Although the final solutions were all completely transparent, their refractive indexes varied. Tabulated values for the refractive indices were taken from a data sheet by the Glycerin Producers' Association [7]. Other properties of the solutions, like viscosity and density, were calculated using an online calculator [8], based on [9] and [10]. The temperature of the fluid was assumed to be a constant, at 25 ° C, as this could not be controlled, due to external factors. Temperature measurements yielded an uncertainty of ±1 ° C. These deviations affect the density and viscosity in turn, effect which will be discussed further in Section 5.2. This data was used throughout the experiment, as neither a refractometer, nor a viscometer were readily available options.

## 3.5 Detailed description of measurement run

While the general act of recording the vibrating bath and logging the $\Gamma$ values has been discussed previously, the complete methodology of taking a measurement is significantly more complex. For every driving frequency that was used, the following measurement runs were completed.

First and most importantly, five recordings of so called 'run-ups' are taken, in order to increase precision. This type of measurement entails starting the recording and the log simultaneously, with the wave generator on stand-by. Afterwards, the amplitude of the oscillation is slowly increased over the span of 15-80 s, depending on how fast the fluid's onset acceleration is reached. In short, the 'run-ups' are used to detect the value of $\Gamma$ for which subharmonic Faraday waves appear, answering the second research question.

The second type of measurement extracts the actual frequency of the Faraday waves. These recordings start after the waves have already stabilised for a given amplitude and they usually span upwards of 10 s. They can be further categorised by the amplitude of the waves or how violent the phenomenon appears to be, as they have been named either 'Highly visible' or 'Chaotic'. The script that analyses these recordings goes over every frame and extracts the frequencies at which the Faraday waves oscillate by applying a Fourier transform, which is why less of these recordings are needed, between one and three per driving frequency, depending on how unexpected the waves behave, displaying complex patterns. A more detailed description of the script and surface reconstruction procedure can be found in Section B.3. This type of measurement is used to answer the first research question, regarding the frequency of the oscillations. It does not require as much cross-referencing with the logged $\Gamma$ values, as the recordings usually concern waves formed past the onset acceleration.

These two types of measurements were taken using the following driving frequencies: 15 Hz, 17 Hz, 20 Hz, 22 Hz, 25 Hz, 27 Hz and 30 Hz, enough to confirm the $n/2$ dependency between the surface standing waves and the provided frequency.

Finally, a third type of measurement was done, in order to achieve the full scope of the FSSS surface reconstruction, extracting wavenumbers. This consisted of varying the driving frequency, using an extended range of $15 - 50$ Hz at a constant concentration of 40% glycerol by weight, and recording the Faraday waves using the same methods as the previous measurement types.

## 3.6 Final setup

A 3D render of the Faraday waves setup that was used is shown below in Figure 6.

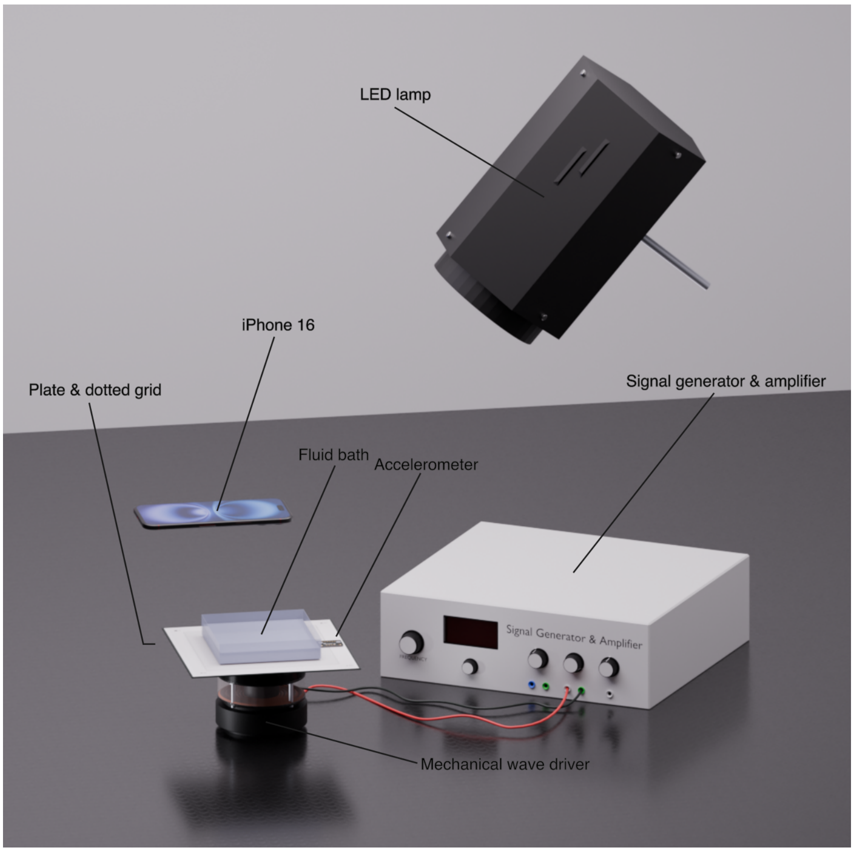


Figure 6: Experimental setup for measuring Faraday waves, modelled in Blender.

# 4 Results

Most of the results can be interpreted visually from the graphs below, however, the raw data can be found in the GitHub of the project in Section C, namely under *artifacts/paper/processed_results*. For Section 4.1 */processed_results/frequency*, for Section 4.2 */processed_results/onset* and for Section 4.3 */processed_results/wavenumbers*.

## 4.1 Subharmonic frequency signatures

Using the methods from Section B.3 across our datasets, we can obtain the necessary information regarding the measured frequencies of the standing waves detected in the videos, particularly by plotting the spectral power $P(f)$ from Equation (35) in different ways.

### 4.1.1 Representative 15 and 20 Hz spectra and comparison

We start by considering 80% glycerol by mass. In Figure 7, we can see the absolute spectral power of the frequencies obtained from the methodology of Section B.3. In the following plots we graphed spectral distributions for both low-forcing ("near-onset") and high-forcing ("well above onset"), though both are already above onset. These are qualitative terms based on the based on the moment Faraday waves were observed at the lab, for some acceleration, and it has the purpose of understanding how the frequency peaks qualitatively vary with higher amplitudes.

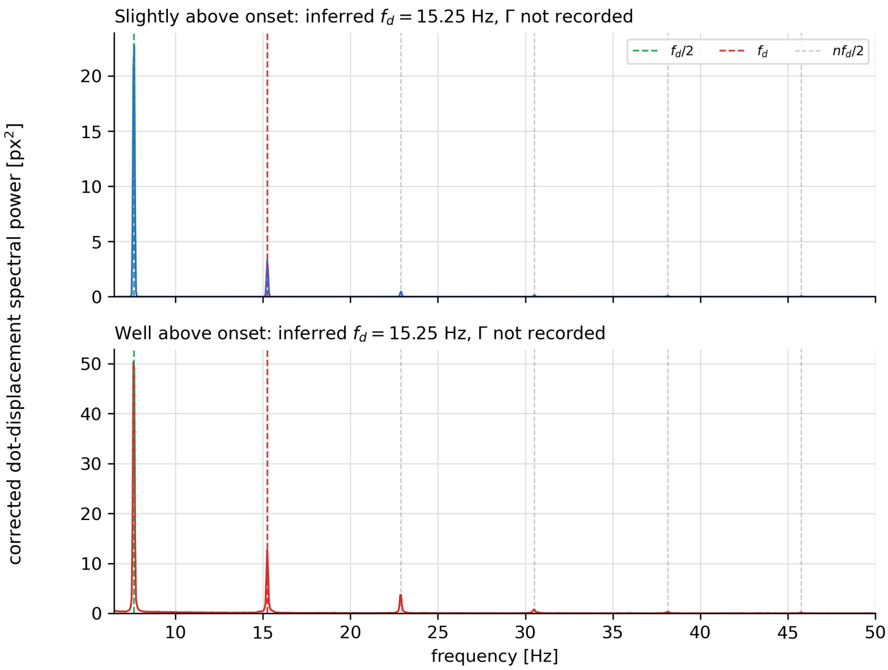


Figure 7: Absolute spectral power for the tested frequencies, particularly for 80% glycerol. Vertical lines are drawn at half-integer harmonic driving-frequency values, where the driving frequency in this case was 15.25 Hz. In this dual graph we have both low-forcing Γ as well as considerably higher-forcing. The Γ value for this graph is purely qualitative (since for this measurement in specific it was not recorded).

For a 20 Hz driving frequency, we obtain Figure 8.

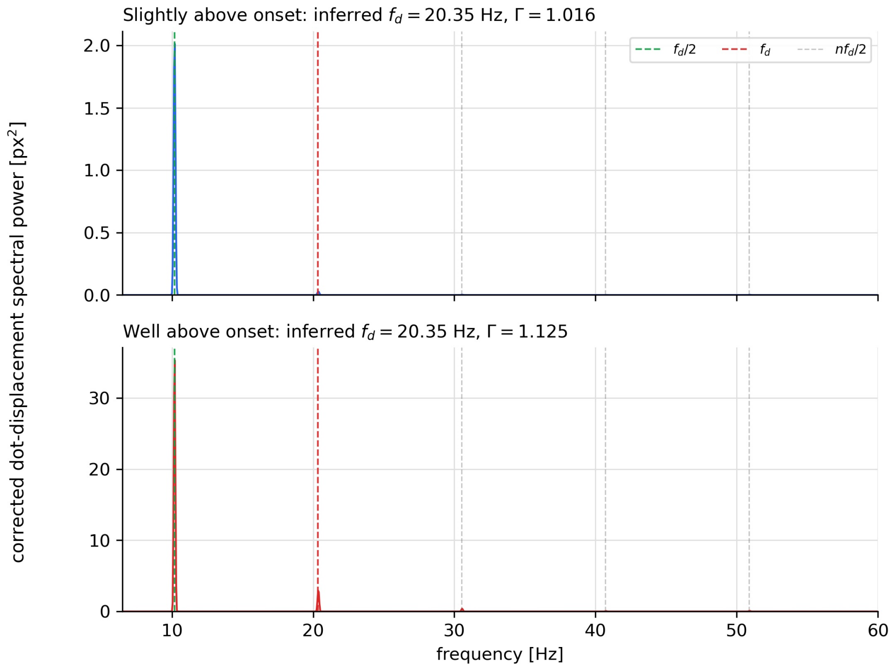


Figure 8: Absolute power for the tested frequencies, particularly for 80% glycerol. Vertical lines are drawn at half-integer harmonic driving-frequency values, where the driving frequency in this case was 20.49 Hz. In this dual graph we have both low-forcing Γ as well as considerably higher-forcing.

More importantly, by plotting the spectral powers on a logarithmic scale, as opposed to Figure 7 and Figure 8, and using the ratios between tested frequency $f$ and $f_d$ on the horizontal axis, we can get the following graphs in Figure 9 and Figure 10.

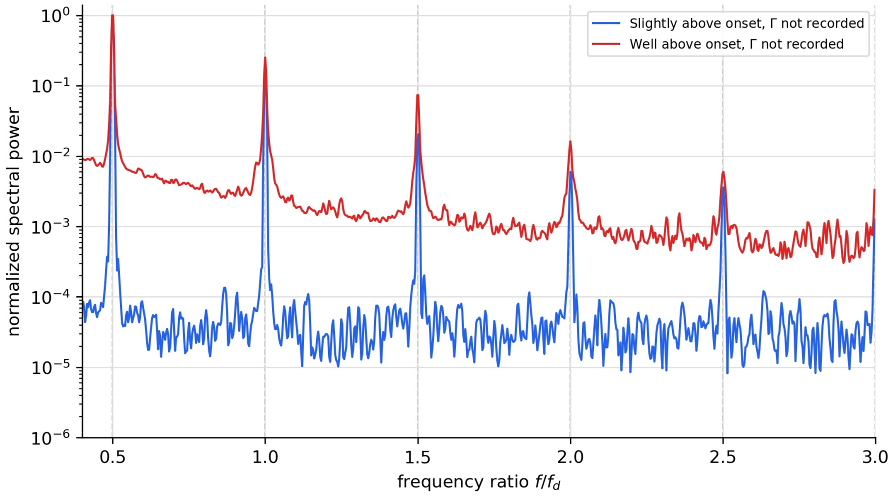


Figure 9: Normalised spectra for 80% glycerol by mass, plotted on a logarithmic scale. This graph shows the relative intensity of the half-integer frequency peaks. This is shown both for low-forcing Γ, and also for a higher value of Γ. The Γ value for this graph is purely qualitative (since for this measurement in specific it was not recorded).

In Figure 9 a total mass of 60 g and concentration of 80% was used, so using Equation (23) with

$\rho_{80\%}$ we get a bath height of 4.965 mm, and for this concentration of 80% by mass: dynamic viscosity of 60.1 cP and kinematic viscosity of $4.97 \times 10^{-5}$ m$^2$ s$^{-1}$.

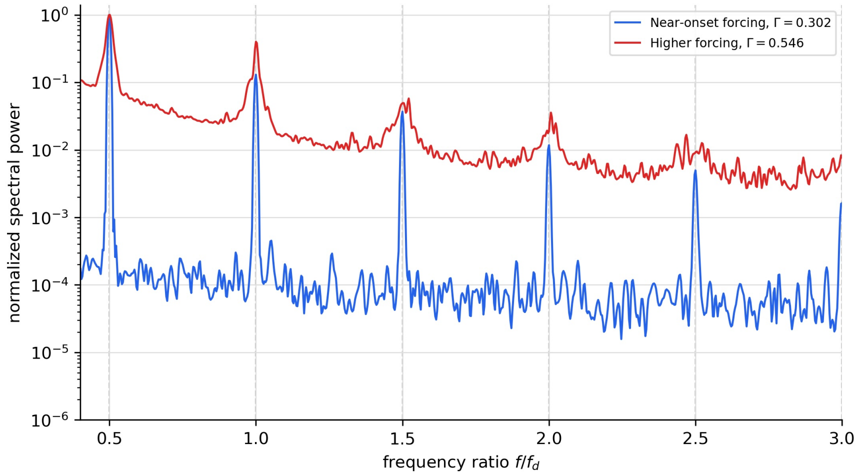


Figure 10: Normalised spectra for 20% glycerol by mass, plotted on a logarithmic scale. This graph shows the relative intensity of the half-integer frequency peaks. This is shown both for low-forcing Γ, and also for a higher value of Γ, relative to onset.

For Figure 10 we used 60 g, with 20 wt% and obtained a bath height of 5.731 mm, for this concentration: dynamic viscosity of 1.76 cP, and kinematic viscosity of $1.68 \times 10^{-6}$ m$^2$ s$^{-1}$.

Finally, beyond varying the viscosity for the same driving frequency, we can vary the driving frequency itself, so, for example, the 80% concentration at $f_d = 20$ Hz can be seen in Figure 11.

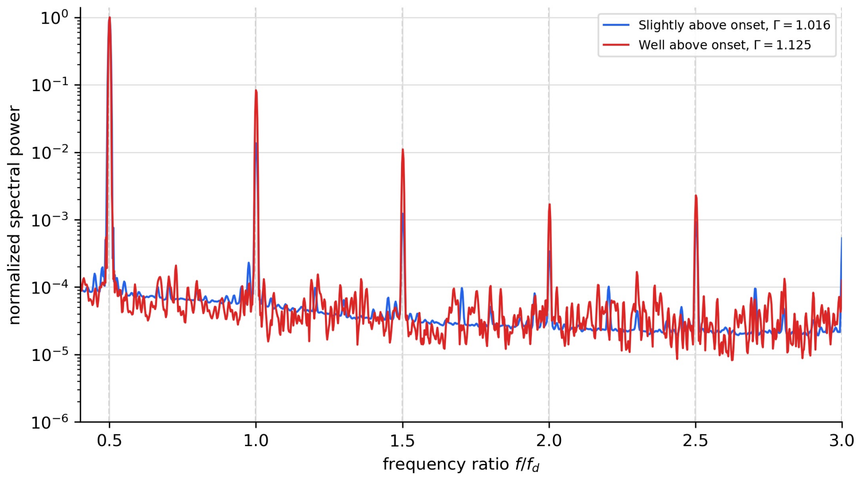


Figure 11: Normalised spectra for 80% glycerol by mass, plotted on a logarithmic scale. This graph shows the relative intensity of the half-integer frequency peaks. This is shown both for lower-forcing, and also for a higher value of Γ

#### 4.1.2 Frequency sweeps at fixed viscosity

Now, we can also plot the spectral lines that were observed in the previous figures but across all used driving frequencies $f_d$, for one fixed viscosity. In the case of 80% by mass, we can observe the plotted heatmap, where the bright lines correspond to high values of $P(f)$.

The vertical axis is divided into "frequency bands", where one specific driving frequency, estimated by fitting the accelerometer's equation of motion Equation (25), corresponds to an entire "vertical width" (which is clear from the difference in background colours).

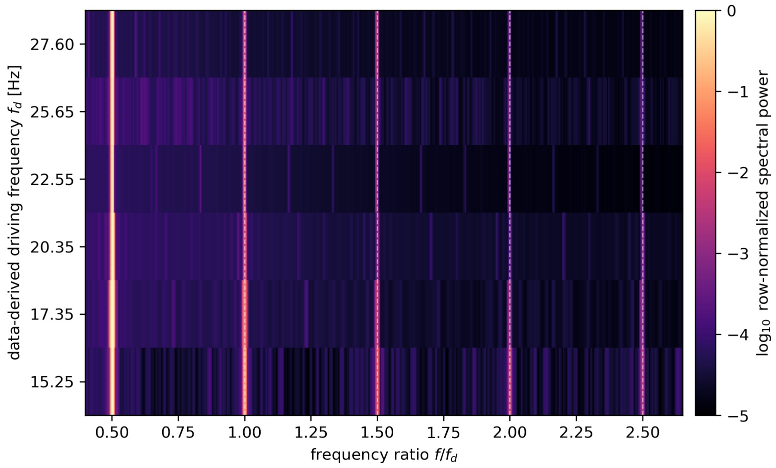


Figure 12: Heatmap for 80% glycerol by mass. Bright lines show a strong frequency signature (log-normalised spectral power close to zero), and dark colours show less relevant relative frequency signatures (log-normalised spectral power close to -5). Horizontal axis shows frequency ratios, relative to the driving frequency. Vertical axis shows driving frequencies used, as thick "bands", which were measured with the accelerometer, thus this is not a "continuous" frequency vertical axis. The heatmap itself is of a normalised $\log_{10}$ (normalised per frequency band/row) mapping, the same as Figure 11.

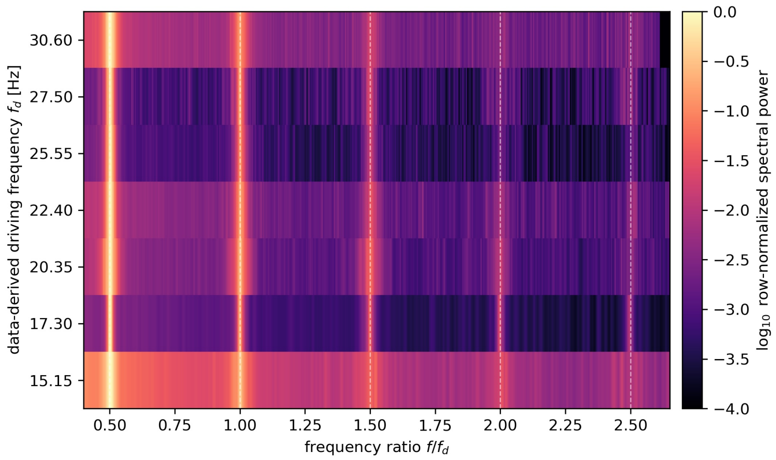


Figure 13: Heatmap for 20% glycerol by mass. Bright lines show a strong frequency signature (log-normalised spectral power close to zero), and dark colours show less relevant relative frequency signatures (log-normalised spectral power close to -5). Horizontal axis shows frequency ratios, relative to the driving frequency. Vertical axis shows driving frequencies used, as thick "bands", which were measured with the accelerometer, thus this is not a "continuous" frequency vertical axis. The heatmap itself is of a normalised $\log_{10}$ (normalised per frequency band/row) mapping, the same as Figure 11. The videos related to this heatmap used the higher range of $\Gamma$, so already well above onset.

### 4.1.3 Dataset-wide subharmonic response

Using the same heatmaps as the previous section, we can construct a single heatmap that encapsulates the entire dataset, for all measured viscosities/concentrations of glycerol and driving frequencies, namely Figure 14.

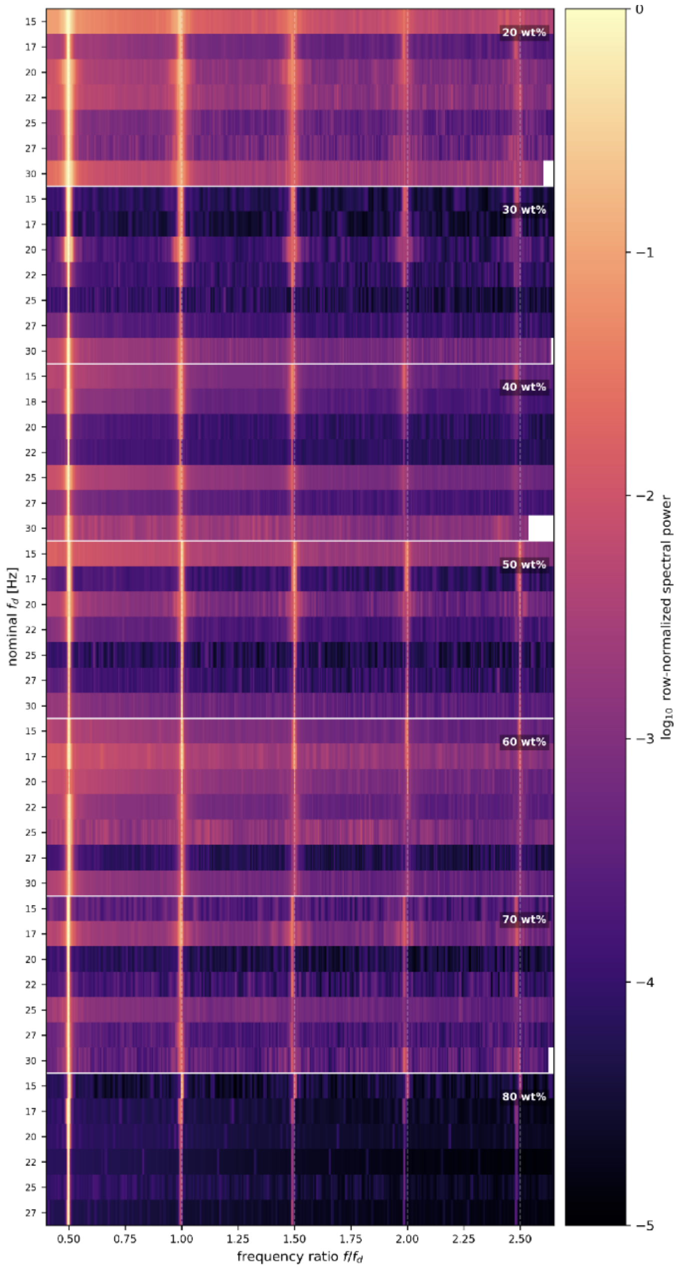


Figure 14: Collection of stacked heatmaps for all of the concentrations measured. Brighter lines show high log-normalised spectral power. Horizontal axis shows the ratio between the frequency on the plot and the driving frequency, and the vertical axis shows the various nominal frequency bands. The heatmap itself is of a normalised $\log_{10}$ (normalised per frequency band/row) mapping, the same as Figure 11.

For clarity, "nominal frequencies" are the frequencies used to "group" a set of measurements, despite the fact that the actual frequency observed in each measurement might have been slightly off. Therefore, despite the bands in Figure 14 having integer values, the actual measurements had values of $f = f_{\text{nominal}} + \Delta f$.

## 4.2 Onset acceleration estimation

Besides extracting frequency spectra from the apparent dot motion, we also found a way to extract the onset acceleration $\Gamma_c$ from the same dot motion, namely by analysing the run-up videos, as mentioned in Section 3, and plotting the spectral power $P(f_d/2)$ from Equation (35) of the subharmonic frequency. At onset the spectral power enters exponential growth, which appears as a clear line, in a logarithmic plot, where the onset was manually chosen to be at the start of the linear relationship. The method used is delineated in its entirety in Section B.4.

### 4.2.1 Frequency dependence at fixed viscosity

As delineated in Section 3 we varied both viscosity and frequency for the measurements of onset acceleration, and thus the first important graph is one where we fix viscosity and vary frequency. This allows us to analyse the frequency dependence observed in the measurements and how it compares to theory.

Both theoretical curves come from Equation (13). The min-k curve comes from minimising $\Gamma_c(k)$ for $k \in \mathbb{R}$ (all values of $k$), and the rectangular-k curve comes, again, from minimising $\Gamma_c(k)$ but $k$ must obey Equation (12).

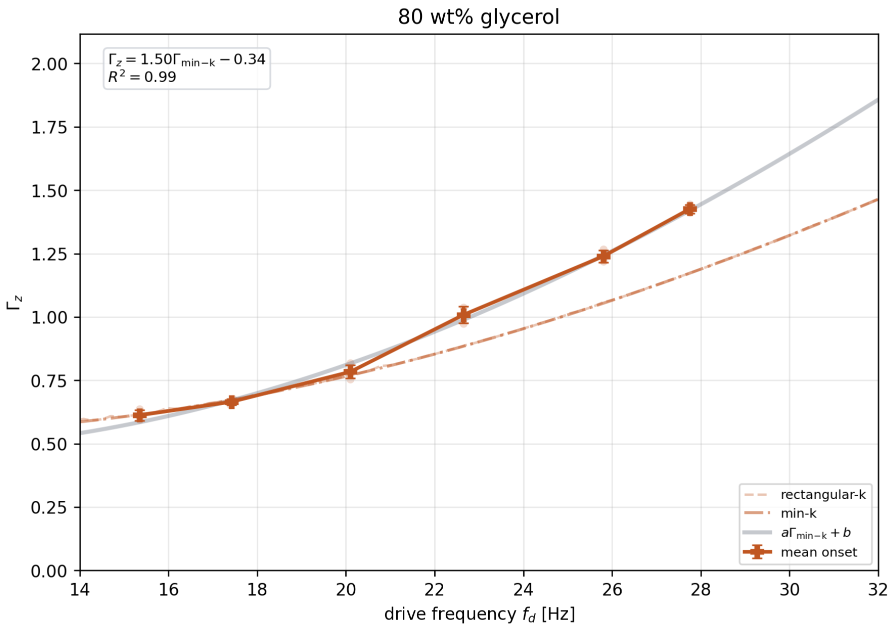


Figure 15: Standalone onset estimates for fixed 80 wt% and frequencies between 15 Hz and 27 Hz. Two theoretical models were plotted, one for min-k onset estimates and another for only valid rectangular-k estimates. Error bars indicate statistical error from repeated measurements.

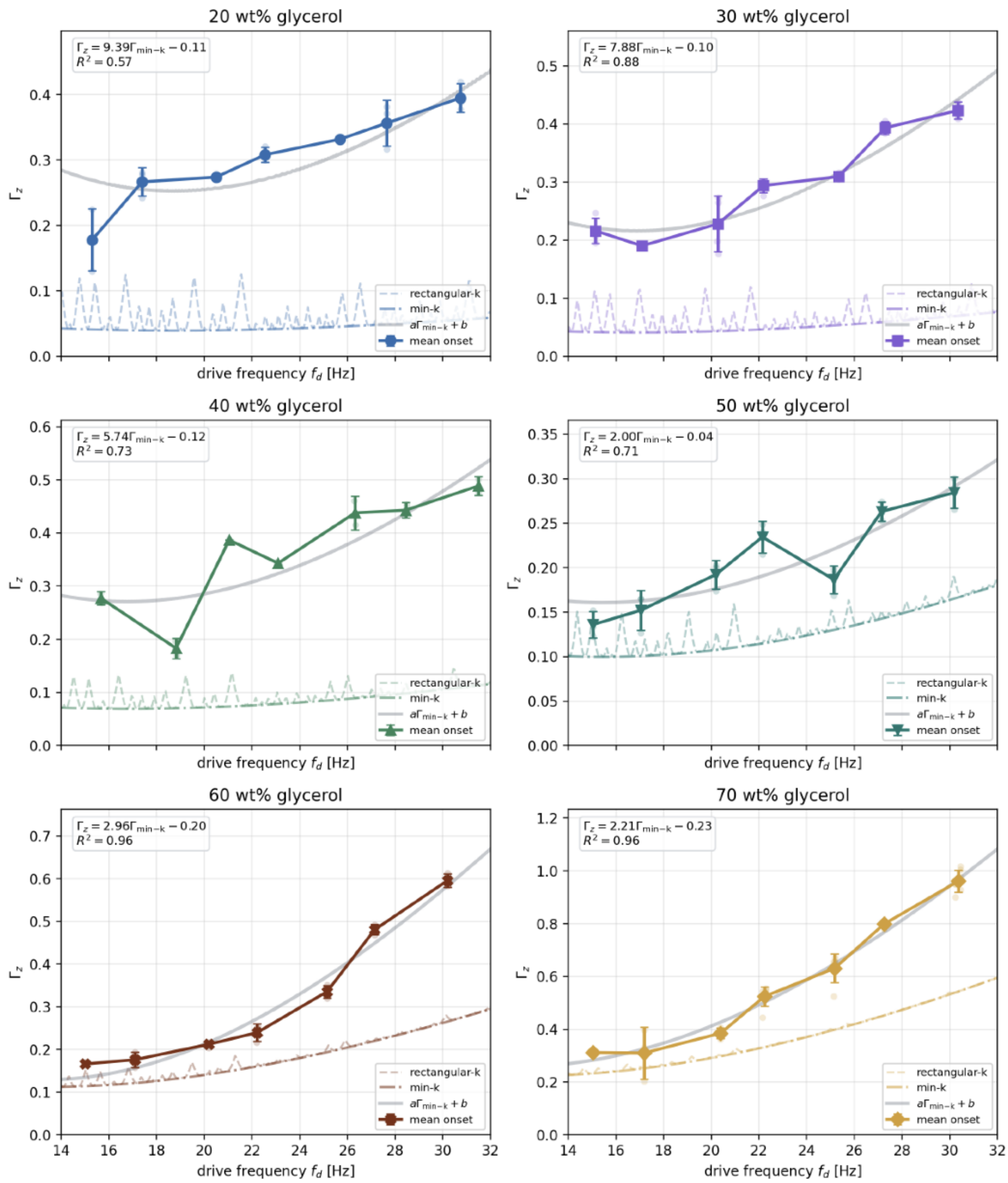


Figure 16: Onset acceleration estimates, for fixed viscosity and variable frequency. Viscosities range from 20 wt% to 70 wt% concentrations, and frequencies between 15 Hz to 30 Hz. Two theoretical models were plotted, one for min-k onset estimates and another for only valid rectangular-k estimates. Error bars indicate statistical error from repeated measurements.

Figure 15 and Figure 16 show the frequency dependence of the estimated onset values compared with the two different theoretical models.

Both restrictions on $k$ were then used to estimate the theoretical values for $\Gamma_c$ by the method described in Section 1, namely by considering a range of valid $k$ values and then calculating the onset from Equation (13), for this range of $k$ values and then picking the $k$ with smallest onset.

Furthermore, a fit of the form $a\Gamma_{min-k} + b$ was performed. The fit simply adds a scaling factor and vertical offset to the theoretical curve, assuming continuous-$k$, giving an idea of the fundamental mathematical dependence of the data points, relative to the theory. See the figures themselves for the values of $a$ and $b$, or Section C for fit values with errors.

#### 4.2.2 Viscosity dependence across the dataset

Naturally, after fixing viscosity and analysing frequency dependence, we can fix frequency and analyse the viscosity dependence of $\Gamma_c$.

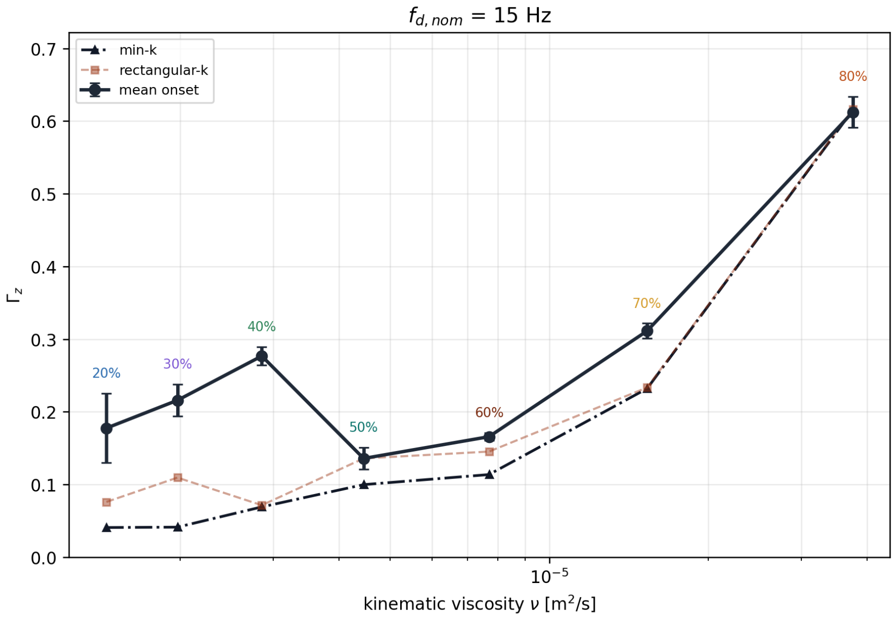


Figure 17: Standalone onset estimates for fixed 15 Hz and variable logarithmic-viscosities. Two theoretical models were plotted, one for min-k onset estimates and another for only valid rectangular-k estimates. Error bars indicate statistical error from repeated measurements.

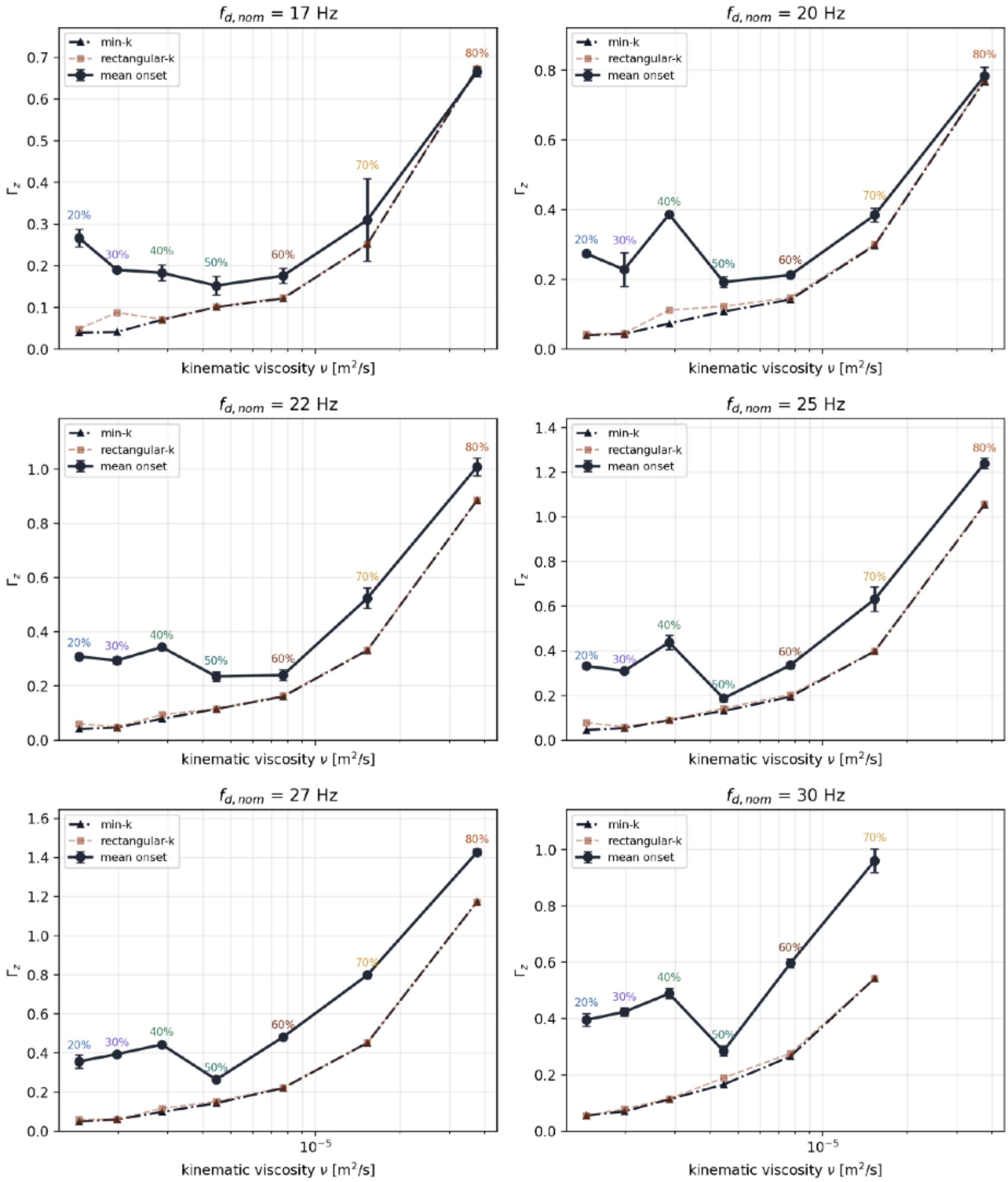


Figure 18: Onset acceleration plotted against logarithmic-viscosity, with fixed frequency. Frequencies range from 17 Hz to 30 Hz and viscosities from 20 wt% to 80 wt%. Two theoretical models were plotted, one for min-k onset estimates and another for only valid rectangular-k estimates. Two important points, first, the 80 wt% run for 30 Hz is missing, since our shaker was not capable of producing the necessary minimum onset for waves to appear, and second, the theoretical curves are not continuous but are discrete/per-measurement, since each viscosity batch of measurements was performed under slightly different conditions, and bath height and mass were not controlled between batches of runs with same viscosity. Error bars indicate statistical error from repeated measurements.

Figure 17 and Figure 18 show the obtained onset acceleration estimates, with both theoretical models graphed, similarly to the results in Figure 16, for fixed nominal frequency bins (this simply means that the measurements are grouped by frequencies that are approximately equal to the integer nominal value, like 20 Hz, however, each measurement may have had a slightly different frequency, depending on the actual value measured by the accelerometer.)

## 4.3 Spatial spectra analysis and reconstruction

For 40 wt%, and in a range of 15 Hz to 50 Hz, we used the methodology described in Section B.5 to both extract the dominant wavenumbers, reconstruct the surface of the fluid, as well as plot the complex temporal amplitudes from Equation (35) for each point over time, for stable runs.

### 4.3.1 Extracted wavenumbers

From the reconstructed surface waves $\zeta(x, y, t)$ (notation defined in Section 1 and Section B.5) we can apply a spatial Fourier transform Equation (45) to obtain the dominant wavenumber $k$, and then by solving the dispersion relation Equation (2) with the subharmonic frequency measured, based on Section B.3, we can find the theoretical wavenumber $k$ that is expected for that frequency. The graph of the measured wavenumbers and expected wavenumbers can be found in Figure 19,

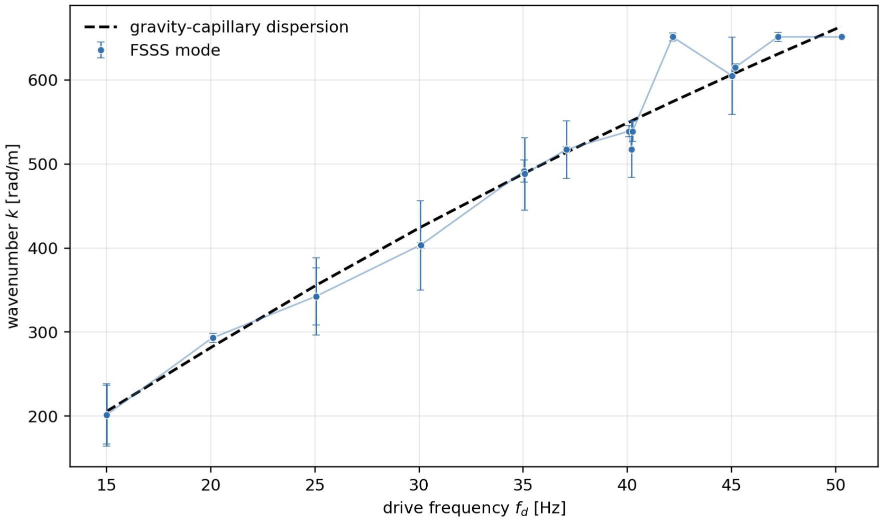


Figure 19: Dominant wavenumbers extracted from reconstructed surface plotted versus respective driving frequency. Dispersion relation Equation (2) is also graphed to compare with the measured wavenumbers. The dispersion relation was graphed by solving for the value of $k$ for the same dominant sub-harmonic frequency as measured. The errors in this graph are not statistical (from repeated runs), they come from the Fourier spatial resolution of the peaks (sub-bin fitting), namely half of the peak's width.

Furthermore, we can graph the measured FSSS wavenumbers and the allowed rectangular wavenumbers, as described in Section 2.4, with Equation (12). This yields Figure 20.

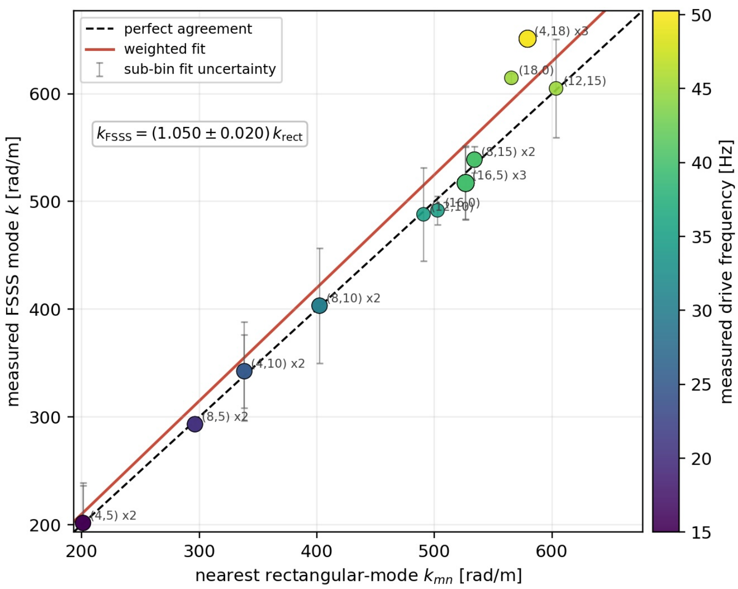


Figure 20: Graph of extracted FSSS wavenumbers $k$ against the closest rectangular mode $k_{mn}$. The colour map indicates the driving frequency related to that extracted wavenumber and the per-point index $(m, n)$ indicates the integer values that calculate the closest rectangular mode $k_{mn}$. The "perfect agreement" line simply graphs $k_{FSSS} = k_{RECT}$, indicating that the values are equal, as they should be in the ideal case. A error-weighted fit of the data points in this graph gave a slope of 1.05 ± 0.02. The errors in this graph are not statistical (from repeated runs), they come from Fourier spatial resolution of the peaks (sub-bin fitting), namely half of the peak's width

### 4.3.2 Reconstructed waves

We can plot the signed height map $\zeta(x, y, t)$ for some time $t$ (some frame), and then by applying a filter over unwanted small and large wavelengths (which explains why some sections are not as colourful) we can obtain Figure 21 and Figure 22.

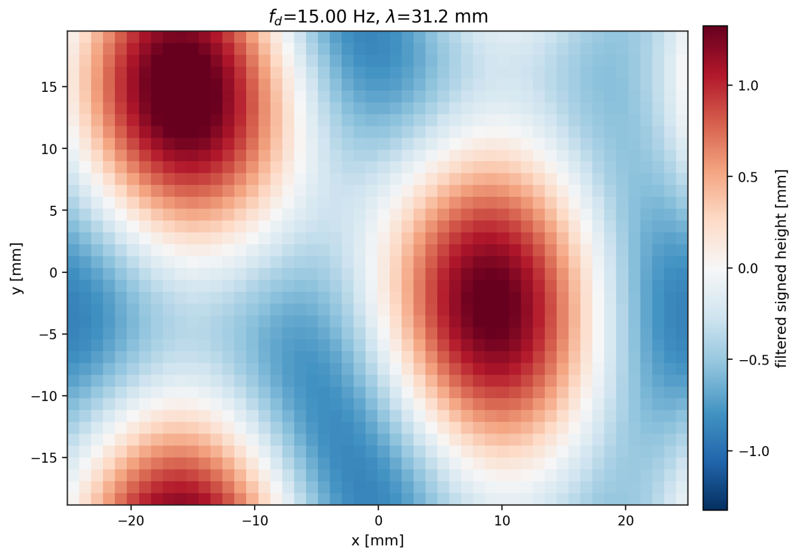


Figure 21: Representative signed height map $\zeta(x, y)$ for 15 Hz, and extracted dominant wavelength. The colourmap represents height in mm of the surface. The same colourmap can be consulted for Figure 22.

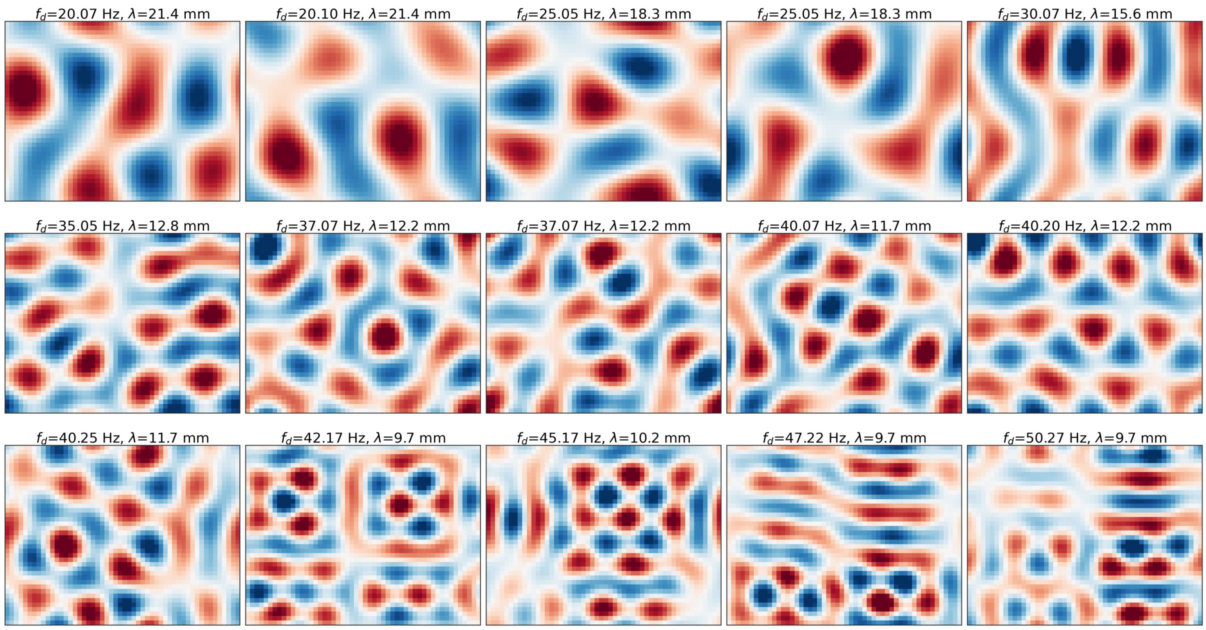


Figure 22: Signed height map grid, for 20 Hz to 50 Hz, of a picked frame from reconstructed Faraday waves. The colourmap represents the signed height, where red colours represent peaks and blue colours represent valleys, as in the colourmap of Figure 21.

#### 4.3.3 2D $f_d/2$ spectral power

By considering the motion of a point on the surface $\zeta(x_i, y_i, t)$, over the course of the entire reconstructed video, one can then use this as an oscillatory function and then find the spectral power of the subharmonic frequency. Figure 23 and Figure 24 show the graph of this spectral power for each point, where dark spots indicate that that point has a very low subharmonic spectral power, whereas bright spots have a high spectral power.

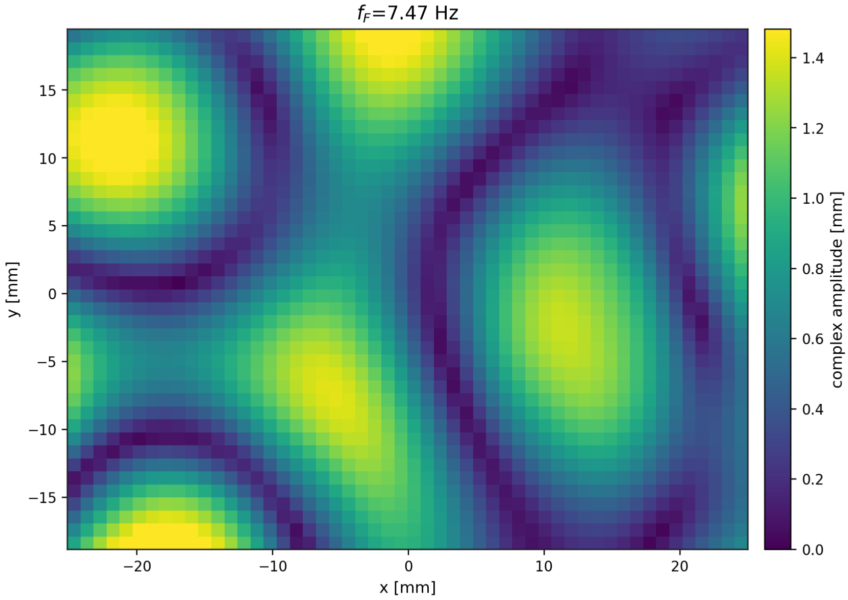


Figure 23: Spectral power (over time) Equation (35) graphed for each point. Dark colouring shows a low spectral power around half-harmonic and bright colouring shows high spectral power around half-harmonic.

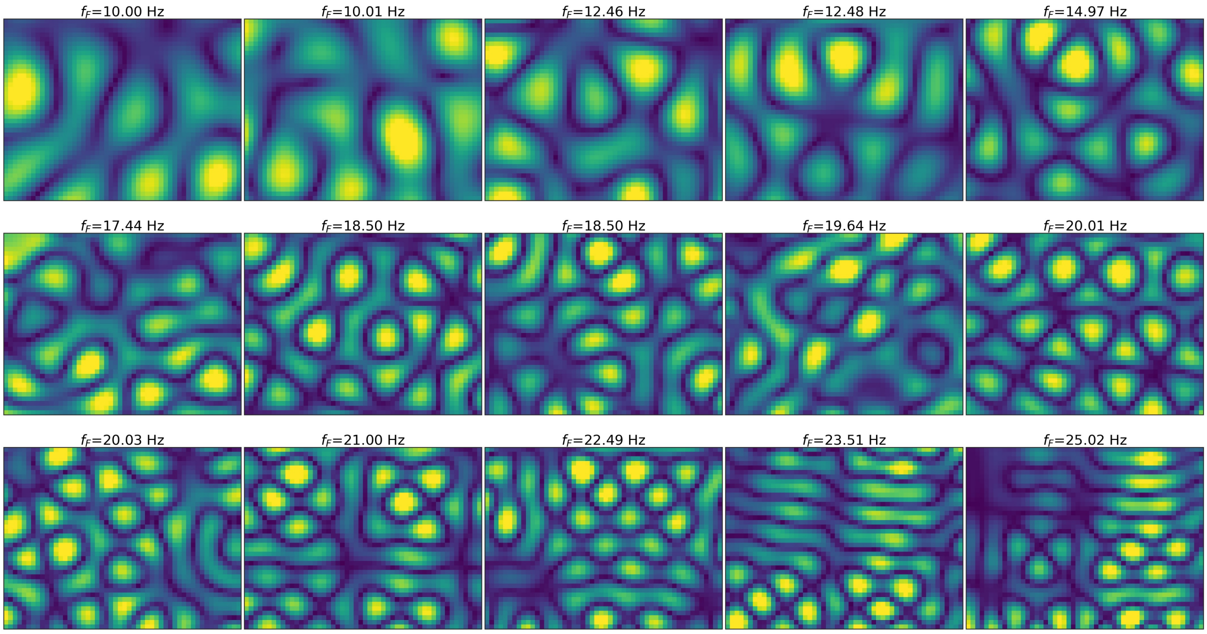


Figure 24: Grid of graphed 2D spectral powers for the remaining reconstructions. Dominant subharmonic frequency can be found at the top of each image. The colour scale can be referenced to Figure 23.

# 5 Discussion

## 5.1 Interpretation of results

From the experimental results, it was found that frequencies corresponding to half-integer multiples of the driving frequency were the dominant occurring frequencies for all driving frequencies tested in every mass fraction of glycerol in water (Figure 14). Since the aim of this experiment was to qualitatively measure the (sub)harmonic behaviour of the Faraday waves, we did not look for exact values and their accompanying errors; the (sub)harmonic peaks usually had a spectral power three or four orders of magnitude higher than other frequencies, indicating that they were the dominant frequency.

This is in line with our hypothesis, based on what is expected from the theory outlined in Section 1, where the aforementioned instabilities in the Mathieu Equation (3) predict that harmonic and subharmonic waves with angular frequencies of the form $\omega_0 \approx \frac{n}{2}\omega_d$ will resonate to outgrow the linear damping and thus become dominant over the other frequencies.

The reason why primarily frequencies with a lower $n$ are dominant is because these require the lowest onset acceleration to appear, as supported by the resonance tongues in Figure 1: acceleration may vary in time and space because of effective gravitational acceleration from Equation (4) and any potential tilt of the plate; this means that sometimes higher accelerations than the minimum needed for Faraday waves are reached; however, the $n = 1$ frequency will always be reached, while higher $n$ may not.

Furthermore, the onset acceleration for which Faraday waves appear generally increases for higher viscosities and driving frequencies, as can be seen in Figure 15, 16, 17 and 18. The onset acceleration increased by a factor of $2.5 \pm 0.3$ on the low end at 17 Hz to $4.0 \pm 0.4$ on the high end at 27 Hz, between a glycerol mass fraction of 20% and 80%. The onset acceleration increased by a factor of $1.8 \pm 0.2$ on the low end at 40% to $3.6 \pm 0.2$ on the high end at 60%, between a driving frequency of 15 Hz and 30 Hz.

According to the hypothesis, the onset acceleration increases with viscosity and frequency according to Equation (10); this is shown in the aforementioned plots by a dashed line. Our results consistently lie above this expected line, although onset acceleration does generally increase with viscosity and frequency and gets closer to the theorised values for lower frequencies and higher viscosities, perhaps more noticeably seen in Figure 15 and Figure 17.

It is worth noting that the data does follow the general trend of our theory, as seen in the previous figures: when we apply a scaling factor $a$ and a vertical translation $b$ for fixed viscosities (as delineated by the grey line in the figures), the measurements seem to match very well. We do this linear transformation to account for any possible deviation in the values for the properties of the solution ($a$) and any kind of minimal acceleration that the shaker has to reach to get it to move at all ($b$). This technique was also used by Pedersen et al. [2], since their results also were above the expected line, though our results lie above the predicted values even more. The scaling factor a ranges from $9 \pm 4$ for the lowest viscosity to $1.498 \pm 0.074$ for the highest viscosity (as seen in Figure 15 and Figure 16), suggesting that values for higher viscosities are more in line with our theory and its assumptions.

This may be due to the fact that lower glycerol concentrations and thus viscosities may create onset accelerations below the minimum acceleration threshold needed to activate the shaker, leading the reconstruction to overestimate the onset acceleration. Furthermore, for higher driving frequencies the amplitude of the waves is too small to be detected by the surface reconstruction, thus needing a higher acceleration to create waves visible for the reconstruction, again leading to an overestimation of the measured onset acceleration. Both of these points are discussed in more detail in Section 5.2.

These significant systematic errors during this part of the experiment make it difficult to definitively confirm or disprove that Faraday waves exactly follow Equation (10); though after attempting to filter some of the errors out using the linear transformation, the results seem to somewhat follow it; particularly the increasing trend is clearly observed.

Finally, the wavenumbers of the dominant waves were predicted to closely follow the dispersion relation in Equation (2). The main wavenumber was predicted to correspond to the most dominant frequency, being $\omega_0 = \frac{1}{2}\omega_d$. From Figure 19 we can see that our results closely follow our hypothesised curve, indicating that they indeed adhere to the dispersion relation.

In addition to that, we observed that these wavenumbers match with the wavenumbers from the rectangular modes. In Figure 21 and Figure 22 (ignoring contamination of the Faraday waves due to various experimental imprecisions, as is further discussed in Section 5.2), we can see that the Faraday waves create peaks in a grid-like pattern. This pattern is more visible and has smaller distances between peaks for higher driving frequencies, though higher driving frequencies also lead to more unwanted contaminating waves, as seen by the wave fronts disturbing the grid pattern.

Interestingly, when observing Figure 23 and Figure 24, we can see that these are "complementary" to the reconstructions. The points of low-spectral power (dark points) match with the points where the surface reconstruction yielded zero height (white points). Naturally, this clearly shows the "standing" nature of the Faraday waves. Since the dark points outline that there was zero sub-harmonic oscillatory motion for the waves, over the time interval of the video, then those points must have been at constant height, over this interval, and only the peaks and valleys of the reconstruction actually were oscillating with the Faraday wave.

As discussed earlier, the theory expects the wavenumber to increase with driving frequency. Indeed, this is what is observed in the figures: higher driving frequencies show a shorter distance between peaks, meaning a higher wavenumber.

The exact accuracy of our hypothesis is seen in Figure 20, where the measured wavenumbers are measured against the expected wavenumbers, with a dashed line corresponding to a perfect agreement, having a slope of 1, being shown. In our case, the fit has a slope of $1.05 \pm 0.02$, very close to 1, supporting our hypothesis.

## 5.2 Sources of error and uncertainty

This experimental setup was quite delicate, which caused there to be a significant amount of sources of error.

First of all, the surface reconstruction is very sensitive to the setup of the camera; the camera being at a slight angle or being at varying heights throughout the numerous experiments, the camera or the container and the plate under it being slightly filthy or the lighting not being perfect can all cause the dots to look differently in the video than they actually are, causing a deviation in the surface reconstruction from the actual waves.

In addition to the camera, the Faraday waves themselves are also very sensitive to external factors. Even a small bump on the table the shaker is sitting on can cause a very noticeable ripple on the surface of the fluid, distorting the patterns. The plate on which the container rests may also not be completely levelled, leading to a varying depth of fluid and not a perfectly vertical vibration of the container, causing unintended waves from interaction with the walls that can contaminate and interfere with any Faraday waves. Higher accelerations also exacerbate any plate tilt meaning that even the slightest tilt will become a source of error for high accelerations. This is also visible in Figure 22, where higher driving frequencies and thus acceleration show more contamination of ideal Faraday waves with ordinary waves. All of these things may affect the results from the surface reconstruction in unpredictable and sometimes significant ways.

It also takes a while for the waves to stabilise, meaning that if a measurement is made too soon after increasing the acceleration, or if the acceleration changes too quickly, the surface reconstruction will not only differ from the actual waves, but will also change over time, as the waves accommodate to the new acceleration. This has a significant effect on the run-up recording, where the onset acceleration was determined; if the knob for amplitude was not turned very slowly, the Faraday waves will lag behind the turning of the knob, causing the reconstructed onset acceleration to be much higher than theoretically calculated.

The affine corrections in the surface reconstruction have also been known to sometimes remove Faraday waves, instead of actual noise, causing the relative intensity of Faraday waves in the Fourier analysis to drop compared to the noise.

For our theory, it was also assumed that the container containing the solutions was perfectly rectangular. However, our container was slightly curved on the edges, leading to an unfavourable deflection of waves, causing distortion in the Faraday waves, again visible in Figure 22.

Furthermore, there are also uncertainties regarding the measurement of certain quantities, such as the temperature and concentration of glycerol in the solution. When preparing the solution, water and glycerol are being mixed together in the desired mass fraction. However, the scale is quite inaccurate and the water splashes when it is poured in; combining that with the fact that part of the solution is left over, the actual mass fraction of water-glycerol may deviate slightly from what we assume. The temperature has also proved difficult to pin down exactly, given that the measurements for temperature were fairly inconsistent, being able to differ about a degree Celsius. Since the kinematic viscosity depends on the density and dynamic viscosity via $\nu = \frac{\eta}{\rho}$ and both of these variables depend on temperature quite strongly, it will increase the error in our measurements.

Repeating what was said in Section 1, the damping coefficient was not determined with high precision. Meniscus damping and wall damping are two sources of damping that were too complicated to take into account for this report. Although these two sources were estimated to contribute less to the damping factor than the sources that were taken into account, it will still have led to a theoretical underestimation of the real gamma factor. This is yet another factor that increased the experimentally determined onset acceleration.

Another quantity that was not exact was the frequency that was read off from the signal generator. After spectral analysis, it was found that the actual driving frequency was always higher than the driving frequency that was read from the signal generator. This does not matter much, since we can retrieve the actual frequency from the surface reconstruction, and directly from the accelerometer.

Then, for high driving frequencies, the amplitude of the created waves would become very small for lower accelerations due to the fast oscillations. This small amplitude caused the surface reconstruction to fail to detect any Faraday waves, meaning that the acceleration had to be increased beyond the actual onset acceleration before the reconstruction could pick up any Faraday waves, leading to a significant overestimation of the measured onset acceleration for high driving frequencies.

Lastly, the shaker and the accelerometer mounted on it had some considerable problems; the most significant is that the shaker is quite weak, meaning that it only really turns on for a minimal acceleration for a certain frequency. This is problematic for solutions with low onset accelerations (low driving frequencies and low glycerol mass fraction), because the onset acceleration may be lower than the minimal acceleration required for the shaker. This means that for such solutions, the onset acceleration is overestimated, often by a significant amount, disturbing a clear relation between frequency and onset acceleration for lower frequencies and glycerol concentrations. Regarding the accelerometer: the cable with which it is connected to the computer slightly pushes the plate down, acting like a downward force, disturbing the ideal movement of the shaker and the acceleration measurements. The accelerometer is also not completely stable on the plate; it may come off the tape slightly when the shaker goes up and its fall back is then damped by the tape again. This effect should be very small, but it is there nonetheless.

Overall, these factors most significantly influence our hypothesis about the relation between onset acceleration and viscosity and driving frequency, generally leading to a significant overestimation of onset acceleration of the Faraday waves compared to what it is actually like. In addition to that, these errors and uncertainties generally cause more noise and unpredictability in our results.

## 5.3 Improvements to experimental setup

To improve the experiment and avoid some of the obstacles we came across, we firstly recommend having a more stable plate and shaker setup. Our plate was mounted on the shaker by a single rod, making it easy for the plate to have some tilt. We recommend having a shaker that itself has a large surface area, eliminating the need for an unstable auxiliary surface. This new shaker should ideally have a very small acceleration threshold to capture low onset accelerations.

Another simple improvement is to use a perfectly rectangular container, removing some contaminating waves created by a curved enclosure.

A recommended way to detect instability for future research, is using a laser pointing to the surface of the liquid. Initially, the first disturbance of the surface of the liquid was intended to be measured with a laser beam reflecting off the surface onto a sensitive photodiode. It turned out that this setup was simply too complicated with the provided materials and budget. The recommendation is to follow a setup similar to Pedersen et al. [2].

In a future experiment, instead of only measuring the Faraday waves while increasing driving acceleration, it is recommended to either measure the waves also when turning down the driving acceleration or increase the driving acceleration with small intervals, leaving each interval unperturbed for 20-30 seconds. The waves can take a while to form due to the initial exponential increase in amplitude of the waves.

One aspect that could also be improved is the storage of the data: since recordings can be up to 30 seconds long at 240 fps, the storage of the electronic devices used to store the recordings and data in can quickly fill up. It is advised to plan around this by freeing up space before taking new measurements to avoid running out of storage during a measurement.

Lastly, it may be useful to consider keeping variables like bath depth, temperature and recording device height constant throughout the experiments. While not strictly necessary, this will make the analysis easier, because one value can universally be used for the data analysis of every measurement session.

# 6 Conclusion

To conclude, the answer to the first research question regarding the harmonic and subharmonic behaviour is that the Faraday waves clearly show harmonic and subharmonic behaviour according to $\omega_0 = \frac{n}{2}\omega_d$, with frequencies corresponding to lower $n$ being more prevalent, in line with our hypothesis.

The second and third research questions about the relation between viscosity and driving frequency and onset acceleration were difficult to answer due to significant sources of error in our experiment, leading to the experimental reconstruction overestimating the onset acceleration of our Faraday waves. Thus, the only thing that can be accurately concluded is that onset acceleration increases with viscosity and driving frequency.

For our last research question, it was found that the relation between the observed angular frequency and wavenumber of the Faraday waves seems to match what is expected from the dispersion relation. The rectangular modes model also agrees with the measured wavenumbers.

In summary, when considering the errors present in our experimental setup, the hypotheses mostly support our findings when considering our systematic errors. To improve the experiment, future researchers should consider using a stronger shaker, a more stable solution for carrying the container on top of the plate and a perfectly rectangular container to reduce systematic errors in their experiment.

# 7 Declaration of AI usage

The following generative AI was used in writing the report:

- GPT 5.5
- Gemini Flash 3.0

AI was used for these purposes:

- Assistance for blender modelling
- Research/finding references
- Debugging and optimising code
- Spelling check

# References


[1] M. Faraday, "Xvii. on a peculiar class of acoustical figures; and on certain forms assumed by groups of particles upon vibrating elastic surfaces," *Philosophical Transactions of the Royal Society of London*, no. 121, pp. 299–340, Dec. 1831, ISSN: 0261-0523. DOI: 10.1098/rstl.1831.0018. eprint: https://royalsocietypublishing.org/rstl/article-pdf/doi/10.1098/rstl.1831.0018/1453165/rstl.1831.0018.pdf. [Online]. Available: https://doi.org/10.1098/rstl.1831.0018.

[2] H. B. Pedersen, A. F. Abildgaard, M. Søtang Jacobsen, and H. Juul, "A modular experimental system for teaching fluid dynamics with faraday waves," *European Journal of Physics*, vol. 44, no. 6, p. 065 002, Sep. 2023. DOI: 10.1088/1361-6404/acf1df. [Online]. Available: https://doi.org/10.1088/1361-6404/acf1df.

[3] K. Kumar and L. Tuckerman, "Parametric instability of the interface between two fluids," *Journal of Fluid Mechanics*, vol. 279, pp. 49–68, Nov. 1994. DOI: 10.1017/S0022112094003812.

[4] J. Rajchenbach and D. Clamond, "Faraday waves: Their dispersion relation, nature of bifurcation and wavenumber selection revisited," *Journal of Fluid Mechanics*, vol. 777, R2, 2015. DOI: 10.1017/jfm.2015.382.

[5] J. Bechhoefer, V. Ego, S. Manneville, and B. Johnson, "An experimental study of the onset of parametrically pumped surface waves in viscous fluids," *Journal of Fluid Mechanics*, vol. 288, pp. 325–350, 1994. DOI: 10.1017/S0022112095001169.

[6] A. Luongo, M. Ferretti, and S. Di Nino, *Stability and Bifurcation of Structures: Statical and Dynamical Systems*. Springer Nature Switzerland AG, Jan. 2023, ISBN: 978-3-031-27571-5. DOI: 10.1007/978-3-031-27572-2.

[7] Glycerine Producers' Association, *Physical Properties of Glycerine and Its Solutions*. New York: Glycerine Producers' Association, 1963. Accessed: May 27, 2026. [Online]. Available: https://www.cleaninginstitute.org/sites/default/files/research-pdfs/Physical_properties_of_glycerine_and_its_solutions.pdf.

[8] C. Westbrook. "Viscosity calculator," University of Reading, Accessed: May 29, 2026. [Online]. Available: https://www.met.reading.ac.uk/~sws04cdw/viscosity_calc.html.

[9] A. Volk and C. Kähler, "Density model for aqueous glycerol solutions," *Experiments in Fluids*, vol. 59, May 2018. DOI: 10.1007/s00348-018-2527-y.

[10] N.-S. Cheng, "Formula for the viscocity of a glycerol water mixture," *Industrial and Engineering Chemistry Research - IND ENG CHEM RES*, vol. 47, pp. 3285–3288, May 2008. DOI: 10.1021/ie071349z.

[11] X. Wang and J. K. Hale, "On monodromy matrix computation," *Computer Methods in Applied Mechanics and Engineering*, vol. 190, no. 18, pp. 2263–2275, 2001, ISSN: 0045-7825. DOI: https://doi.org/10.1016/S0045-7825(00)00243-7. [Online]. Available: https://www.sciencedirect.com/science/article/pii/S0045782500002437.

[12] K. Takamura, H. Fischer, and N. R. Morrow, "Physical properties of aqueous glycerol solutions," *Journal of Petroleum Science and Engineering*, vol. 98-99, pp. 50–60, Nov. 2012. DOI: 10.1016/j.petrol.2012.09.003. [Online]. Available: https://doi.org/10.1016/j.petrol.2012.09.003.

[13] F. Moisy, M. Rabaud, and K. Salsac, “A synthetic schlieren method for the measurement of the topography of a liquid interface,” *Experiments in Fluids*, vol. 46, no. 6, pp. 1021–1036, 2009. DOI: 10.1007/s00348-008-0608-z. [Online]. Available: https://doi.org/10.1007/s00348-008-0608-z.

[14] S. B. Dalziel, G. O. Hughes, and B. R. Sutherland, “Whole-field density measurements by synthetic schlieren,” *Experiments in Fluids*, vol. 28, no. 4, pp. 322–335, 2000. DOI: 10.1007/s003480050391. [Online]. Available: https://doi.org/10.1007/s003480050391.

[15] G. Bradski, “The opencv library,” *Dr. Dobb's Journal of Software Tools*, 2000. [Online]. Available: https://opencv.org/.

[16] Z. Zhang, “A flexible new technique for camera calibration,” *IEEE Transactions on Pattern Analysis and Machine Intelligence*, vol. 22, no. 11, pp. 1330–1334, 2000. DOI: 10.1109/34.888718. [Online]. Available: https://doi.org/10.1109/34.888718.

[17] N. Otsu, “A threshold selection method from gray-level histograms,” *IEEE Transactions on Systems, Man, and Cybernetics*, vol. 9, no. 1, pp. 62–66, 1979. DOI: 10.1109/TSMC.1979.4310076. [Online]. Available: https://doi.org/10.1109/TSMC.1979.4310076.

[18] F. J. Harris, “On the use of windows for harmonic analysis with the discrete fourier transform,” *Proceedings of the IEEE*, vol. 66, no. 1, pp. 51–83, 1978. DOI: 10.1109/PROC.1978.10837. [Online]. Available: https://doi.org/10.1109/PROC.1978.10837.

[19] D. G. Lowe, “Distinctive image features from scale-invariant keypoints,” *International Journal of Computer Vision*, vol. 60, no. 2, pp. 91–110, 2004. DOI: 10.1023/B:VISI.0000029664.99615.94. [Online]. Available: https://doi.org/10.1023/B:VISI.0000029664.99615.94.

[20] M. A. Fischler and R. C. Bolles, “Random sample consensus: A paradigm for model fitting with applications to image analysis and automated cartography,” *Communications of the ACM*, vol. 24, no. 6, pp. 381–395, 1981. DOI: 10.1145/358669.358692. [Online]. Available: https://doi.org/10.1145/358669.358692.

[21] P. Virtanen et al., “Scipy 1.0: Fundamental algorithms for scientific computing in python,” *Nature Methods*, vol. 17, pp. 261–272, 2020. DOI: 10.1038/s41592-019-0686-2. [Online]. Available: https://doi.org/10.1038/s41592-019-0686-2.

[22] H. Li, M. Avila, and D. Xu, “A single-camera synthetic schlieren method for the measurement of free liquid surfaces,” *Experiments in Fluids*, vol. 62, no. 11, p. 227, 2021. DOI: 10.1007/s00348-021-03326-0. [Online]. Available: https://doi.org/10.1007/s00348-021-03326-0.

# A Floquet theory

This entire section was based on chapter 13 of [6]. To build a computational model that can calculate instability numerically, a mathematical way of showing instability is necessary. The mathematical branch Floquet theory gives us a way to do this. The so-called monodromy matrix is important to us. A monodromy matrix tells us what happens to a set of solutions when the time increases by one period. It is defined with the fundamental matrix, it will be shown in a minute. The fundamental matrix is the solution matrix to a system of homogeneous linear differential equations. These lecture slides were also used as a reference for the following theory. The fundamental matrix will be called $\phi(t)$ and for a 2x2 system of coupled differential equations can be written as:

$$\phi(t) = \begin{bmatrix} x_1(t) & x_2(t) \\ y_1(t) & y_2(t) \end{bmatrix} \tag{15}$$

Floquet theory analyses homogeneous linear differential equations with periodically repeating coefficients. That means:

$$x^{[n]}(t) + a_{n-1}(t)x^{[n-1]}(t) + \ldots + a_1(t)x'(t) + a_0(t)x(t) = 0 \tag{16}$$

with $a_k(t)$ periodic functions. It is clear that a system like this is just an nxn system of coupled differential equations, as the terms are related by $x^{[k]}(t) = \frac{d}{dt}x^{[k-1]}(t)$ so that a vector like the following is found:

$$\frac{d}{dt}\begin{bmatrix} x(t) \\ x'(t) \\ \ldots \\ x^{[n-2]}(t) \\ x^{[n-1]}(t) \end{bmatrix} = \begin{bmatrix} 0 & 1 & 0 & \ldots & 0 & 0 \\ 0 & 0 & 1 & \ldots & 0 & 0 \\ \ldots & \ldots & \ldots & \ldots & \ldots & \ldots \\ 0 & 0 & 0 & \ldots & 0 & 1 \\ -a_0(t) & -a_1(t) & -a_2(t) & \ldots & -a_{n-2}(t) & -a_{n-1}(t) \end{bmatrix} \begin{bmatrix} x(t) \\ x'(t) \\ \ldots \\ x^{[n-2]} \\ x^{[n-1]} \end{bmatrix} \tag{17}$$

It turns out that there will be a solution of the form:

$$X(t) = e^{Bt}P(t), \tag{18}$$

with $X(t)$ the matrix containing all linearly independent solutions for $x(t)$ and all its derivatives, $P(t)$ a periodic function, and $B$ a time-independent matrix. A periodic function is of the form:

$$P(t+T) = P(t), \tag{19}$$

with $T$ the period of the function.

It is clear from Equation (16) that the Mathieu equation can be analysed with Floquet theory.

The monodromy matrix of a system is defined as:

$$M = \phi(T)\phi^{-1}(0), \tag{20}$$

with $M$ the monodromy matrix, $\phi$ the fundamental matrix and T the period of the periodic function in the solution. It turns out that:

$$\phi(t+T) = M\phi(t). \tag{21}$$

From linear algebra, we know that if one of the eigenvalues of this monodromy matrix is greater than one, the matrix will explode over t: instability.

This is exactly what the goal was: a way of mathematically finding instability. Now writing out the Mathieu equation in matrix form gives:

$$\frac{d}{dt}\begin{bmatrix} \zeta(t) \\ \zeta'(t) \end{bmatrix} = \begin{bmatrix} 0 & 1 \\ -\omega_0^2(1 - F\cos(\omega_d t)) & -2\gamma \end{bmatrix} \begin{bmatrix} \zeta(t) \\ \zeta'(t) \end{bmatrix} \tag{22}$$

with $\gamma$ as in Equation (8) and $F$ as in Equation (6). This differential equation can be numerically approximated. In a computational model, the fundamental matrix can be found by numerically by integrating $\phi(t)$ from $t = 0$ to $t = T$, with as starting condition $\phi(0) = I$. With this solved Mathieu equation, the monodromy matrix can be calculated with Equation (20).

# B Data Processing

The goal of this section is to purposefully go into more depth on the computational methodologies that were used to process the videos into temporal and spatial spectra, as well as effectively reconstruct the surfaces with FSSS. The motivation for this is justified since these methods, despite being used regularly, are hardly ever truly explained deeply by the literature, or made open-source.

## B.1 Small dependencies for data processing

After having collected the raw data, namely the videos of stable configurations of Faraday waves as well as run-up videos, we can start processing this data into something coherent. However, we should take time to calculate everything that we will need beforehand.

For each of the concentrations of glycerol we must know the height of the fluid in the bath, this can be calculated using the density of the solution, its total mass and the $100 \times 100\,\mathrm{mm}^2$ geometry of the bottom of the bath. Calculation in this case is easier than direct measurement, since the small height of $\approx 5\,\mathrm{mm}$ would lead to a less precise measurement with a Vernier caliper.

Namely, for a known density $\rho$ and total mass $m$ we find the height of the bath with:

$$V = \frac{m}{\rho} \Rightarrow h = \frac{m}{\rho A} \tag{23}$$

where $A$ is the area of the bath and $V$ is the total volume.

The density, viscosity as well as refractive index used in the processing of the data can be referenced from the data sheet written by the Glycerin Producers' Association [7], as well as Takamura's paper for surface tension estimates [12], and the online calculator, based on [9] and [10], as mentioned earlier in Section 3.4. The temperature of the room was measured to be $25 \pm 1\,^\circ\mathrm{C}$ using a PASCO wireless temperature device. For values not clearly measured in the cited research papers we used simple linear interpolation, based on the values that were measured, to obtain estimated values.

After obtaining the height, density, viscosity and refractive index, we can start preparing the videos themselves for analysis.

The first stage is to use the flat liquid reference video (only first frame), which was taken in the lab, to choose a valid ROI (region of interest), this is a tuple of $[x_{center}, y_{center}, width, height, rotation]$, which delineates the region of the video to be tracked, in dimensions of pixels.

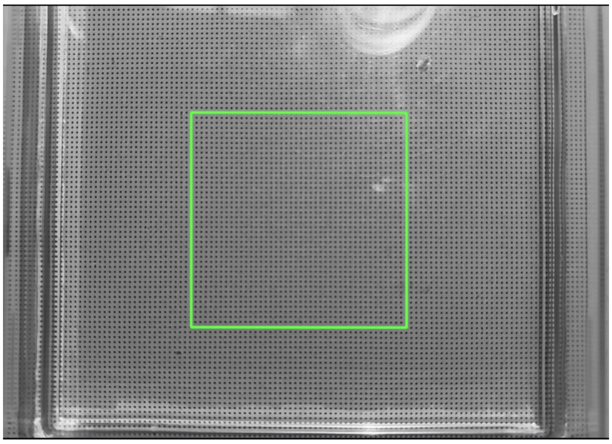

Figure 25: Example of ROI selection for one flat liquid reference

In Figure 25 we can see an example of a chosen ROI for one of the batches. Naturally we could choose different ROIs for each video but that would take an incomprehensible amount of time, and thus we assume that the camera position, luminosity and other relevant factors are constant not only throughout the whole video itself but throughout the entire lab time (this is a valid assumption since the setup barely changes during the measurements - this is why we have only a single flat liquid reference visual, per batch of runs)

The goal of the ROI is to be a region where the most individual dots are clearly visible and contrast sufficiently to be identified by the tracking script. As we can see in Figure 25 this is not a perfect ROI selection, given that we have a small region on the right with a bright spot, due to reflection. Not only that but camera intrinsics play a role, a camera from an iPhone has significant distortions, especially along the borders of the screen, this is why, usually, the ROI selection is centered, even if that costs 10 dots. The cost of a non-uniform dot distance, due to distortion, is much, much larger than dropping 10 dots due to a bright spot.

Larger ROIs lead to more data points for both frequency analysis, surface reconstruction and especially as a more accurate way to calculate the value of the wavelength. However, a smaller ROI with near uniform distance between dots is still preferred, even for wavelength calculations.

Finally, there is one remaining point to touch, namely camera calibration. Obviously, the less distorted the image from the camera the better the results, this is particularly important for FSSS (Free-Surface Synthetic Schlieren - This is a photogrammetry technique to reconstruct exact geometries of fluid interfaces with the dot grid submerged in the fluid - this will be further explained later) [14] [13] . For simple frequency spectral analysis (detecting significant frequencies present in the video - used for testing subharmonic behaviour of Faraday waves) as well as estimation of onset dimensionless acceleration $\Gamma = a_c/g$ for the Faraday waves, the high calibration is not entirely necessary since these quantities are calculated via temporal spectra, so we can leave units in pixels, but for quantities like the wavelength $\lambda$ this is of utmost importance.

To calibrate the camera we used the very common and standard procedure, namely, using a checkerboard pattern and a video of multiple angles of this checkerboard [16]. Then from this video about 100 frames, which were not blurred, and clearly showed the checkerboard, were chosen and using the standard Python package for computer vision OpenCV [15], we used *cv2.findChessboardCorners()* to define the plane of the checkerboard for each frame, and finally we used *cv2.calibrateCamera()* to extract the camera matrix,

$$\mathbf{K} = \begin{pmatrix} f_x & 0 & c_x \\ 0 & f_y & c_y \\ 0 & 0 & 1 \end{pmatrix} = \begin{pmatrix} 1382.64 & 0 & 944.19 \\ 0 & 1380.15 & 565.02 \\ 0 & 0 & 1 \end{pmatrix} \tag{24}$$

With this camera matrix we can "undistort"(or, more accurately, understand where the distortions lie) to robustly choose ROIs and also guarantee uniform dot distances, proper 1 mm (distance between dots) to pixel ratio for FSSS and solving for camera position.

One small, simple but adjacent point is extracting the data measured by the ADXL345 (accelerometer). This is easily done with curve fitting.

We can assume that the bath motion is sinusoidal and thus the acceleration will have the same oscillatory motion as well,

$$x \approx A\cos(2\pi f_d t + \delta) \Rightarrow a \approx \Gamma\cos(2\pi f_d t + \delta) \tag{25}$$

So by fitting the equation of acceleration values we can then extract the fit coefficients, namely $\Gamma$ and the driving frequency $f_d$, which should not be trusted from the signal generator, but measured directly from the vertical motion.

On another note, it is quite common that a truly good fit cannot be found which usually underestimates the amplitude of the sine wave, in those cases we consider the envelope of the sample, namely, half of the sum of total "height" of the sample, this gives the amplitude, which is gamma $\Gamma$.

## B.2 Dot tracking over time

Now that we have the selected ROI, we can start tracking the dots themselves. First we must create an indexed grid of dots for the flat reference grid, which we will use to find the relative displacements of the dots.

To do this we begin with very standard OpenCV image processing to extract the dots themselves from the frame, first using DoG (Difference-of-Gaussians-like spatial filtering) [19] to enhance the image, which was first converted to grayscale, and then turned into a negative image with bright white blobs, maximising contrast with the dark background, as we can see in Figure 26,

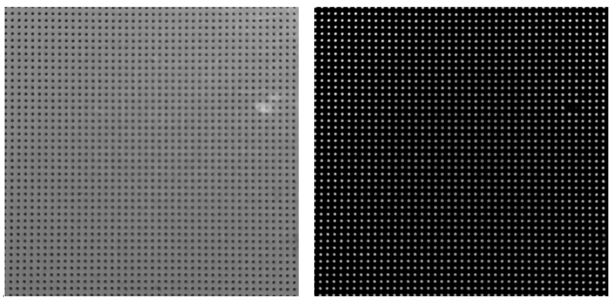

Figure 26: Using DoG (Difference-of-Gaussians-like spatial filtering) for increasing the visibility of the dark blobs. Left image is a simple grayscale and the right image is "post-DoG"

From here we use Otsu thresholding [17], which works perfectly with the already high contrast image, allowing us to separate the background from the "foreground", namely the dots themselves. This simply means that we now know what pixels correspond to dots and what pixels correspond to the background, by assigning a binary value to all pixels, if the brightness of the pixel is higher than the threshold $T$, it becomes a value of 1 and 0 otherwise.

After that we run a simple *cv2.connectedComponentsWithStats()* which takes the binary pixel grid and then separates all connected components into different objects. Since the dots are completely disconnected we effectively separate the simple binary grid into a set of arrays of pixels corresponding to each dot.

After having the position of each dot (as its center), next comes the interesting part which is effectively indexing all the dots from the flat reference image, into a single connected grid. We do this by using *scipy.spatial.cKDTree()* [21] and local graph propagation. The idea is that we pick a detected dot position, assign it an arbitrary index $(i, j)$, and then we use *scipy.spatial.cKDTree()* to find the neighbours of this dot. After taking the vector displacement between the two points and then comparing to see if it aligns with the $\pm x$ or $\pm y$ directions, we can know if the neighbouring dot is on the left, right, top or bottom relative to the $(i, j)$ dot. Then we propagate the index respectively, so $(left, right, top, bottom) \to ((i-1, j), (i+1, j), (i, j+1), (i, j-1))$ , then we repeat the propagation and we set an anchor point like $(i, j) = (0, 0)$ and thus now all dots are indexed in a grid. We can see the end result in Figure 27,

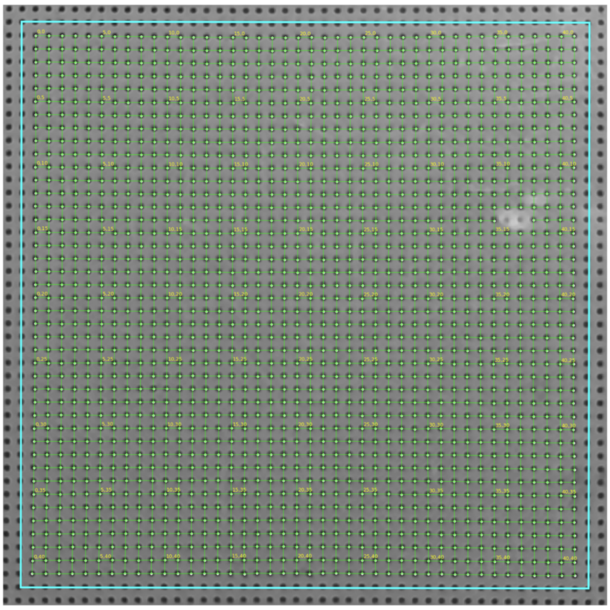

Figure 27: Grid indexing from selected ROI. Green lines show expected pixel distance between dots; yellow lines show larger distances; red lines show very large distances (but these were not present in this ROI selection). Furthermore, yellow tuples $(i, j)$ represent the 2D index of the points, in the indexed grid. Finally, we can see that the points around the bright spot were not recognised, and thus dropped.

With the grid in place we now have a reference of what the dot grid looks like, mathematically, when the fluid is stable, meaning that if the dots move we can find the relative displacement between both positions. One important point to note is that our camera with a distance of $\approx 12.5\,\text{cm}$ relative to the dot grid, allowed us to get around $12.4\,\text{px}$ of separation between the dots, this is a good enough distance to allow for the dots to actually have enough pixel resolution to move around with certain precision.

Now we can move on to actually tracking the dots throughout the video, as they move around. The technique we used is quite simple, we exploited OpenCV's *cv2.matchTemplate()*. Instead of re-indexing the whole grid for every frame, we did a local search, per dot. We first defined a search radius around the reference dot $(x, y)_{ref}$, which depending on the video was about 5–8 px of radius. Then we used *cv2.matchTemplate()* for every point in the search region. This gave us the position of the moved dot $(x, y)_{mov}$ in the search region and thus the displacement relative to the reference grid, $(\Delta x, \Delta y) = (x, y)_{mov} - (x, y)_{ref}$. With this method we can repeat it for every frame of the video and effectively find the relative displacement of each indexed dot over time/frames.

Finally we need to do a small adjustment, otherwise the surface reconstructions as well as frequency spectral analysis yield results full of "noise". The reason for this is that we need to account for global affine transformations, mainly due to, but not exclusively, the motion of the bath itself, which slightly increases/decreases the magnification and position of the dots for different frames. By removing global affine transformations we are ensuring, to a higher degree at least, that the motion we are effectively picking up is from the waves distorting the dot grid, and not from external factors.

We can do this very simply from OpenCV as well, particularly with the method *cv2.estimateAffinePartial2D()*, which uses the RANSAC method [20]. This gives the global affine transformation of the grid, and then we define the "corrected field"

$$(\Delta x, \Delta y)_{corrected} = (\Delta x, \Delta y) - \delta(x, y)_{affine} \tag{26}$$

where $\delta$ is the affine displacement field, basically it represents the displacement of the dots if there were no waves, so we subtract this affine transformation which "cleans" any global movement and only leaves the actual displacement we desire.

Finally, we have a proper dot position for every frame, and we can start analysing what these dot movements actually mean.

## B.3 Frequency Spectral Analysis

The output from the tracking stage was an affine-corrected displacement field $(\Delta x_i(t), \Delta y_i(t))$, which is time-dependent over the video. The goal of this section is to use Fourier analysis to extract the relevant frequencies in the dot motion.

The first important point is that, for now, we are concerning ourselves with the "stable videos", not the run-up videos as referenced in Section 3.

We start by actually transforming the displacement fields into something more usable for Fourier analysis. Despite correcting for affine transformations, which are global, each dot may still have some kind of extra movement and this kind of movement appears in the frequency-domain of the displacement fields as a large combination of low frequency significance, which is not ideal for obtaining the actual significant frequency peaks. Thus, we "center" each dot, indexed with $i$, individually by subtracting its mean displacement over time, yielding the usable field,

$$(\tilde{u}_x, \tilde{u}_y)_i = (\Delta x(t), \Delta y(t))_i - (\text{median}(\Delta x(t))_i, \text{median}(\Delta y(t))) \tag{27}$$

With a proper displacement field the idea will be to project both x and y motion into a complex wave, at various frequencies and then by extracting the complex amplitude of these projections we effectively get a proxy for "how significant is this frequency for the motion of the displacement fields?" - This is the spectral power $P(f)$.

A complex wave for projection can be defined as,

$$c(t) = Ce^{-i(2\pi f t)} \tag{28}$$

where $C$ is the complex amplitude. The minus sign is there because fundamentally we will be testing the motion of $\tilde{u}_x$ against the complex wave, so if we assume that $\tilde{u}_x$ oscillates in the same frequency as our complex wave we can write it as $\tilde{u}_x = Ae^{2\pi i f t}$, and thus, when we project onto the complex "test" wave,

$$Ae^{2\pi i f t} \times e^{-2\pi i f t} = A \tag{29}$$

And the entire amplitude is perfectly extracted. But if the test frequencies were different then there would still be a time-dependent term in the extracted "amplitude".

More explicitly, if $f_0$ is the frequency of the motion and $f$ is the frequency that we are "testing", then

$$Ae^{2\pi i f_0 t} \times e^{-2\pi i f t} = Ae^{2\pi i (f_0 - f) t} \tag{30}$$

This time-dependent term would average to $\approx 0$ over one period. So by integrating over one period we are basically setting the value of Equation (30) to zero if $f_0 \neq f$. Generalising this idea we can define the complex amplitude, in integral form, and then write it in discrete form,

$$C(f) = \frac{1}{T} \int_0^T x(t) e^{-2\pi i f t} dt \Rightarrow \frac{1}{T} \sum x(t_n) e^{-2\pi i f t_n} \Delta t \tag{31}$$

This equation simply states that the complex amplitude will be the average sum of the product between motion and complex wave at some test frequency $f$. This is the standard Fourier transform from time to frequency domain.

With this in mind there is one important correction that is pertinent for our case, namely the Hann window [18] . Fourier transforms assume that our motion is periodic across all time, and it does not take into consideration that at the start of our video we could have a different phase than at the final frame. This leads to what is called "spectral leakage", the idea is that certain frequency peak's spectral power gets "leaked" into other frequencies.

So the idea of the Hann window is to transform the time average of the Fourier transform Equation (31) into a weighted average that decreases significance of the starting and ending frames. Thus we can define the corrected discrete Fourier transform for both x and y as,

$$C_{x,i}(f) = \frac{2}{\sum_t w(t)} \sum_t w(t) \tilde{u}_{x,i}(t) e^{-2\pi i f t}, \tag{32}$$

$$C_{y,i}(f) = \frac{2}{\sum_t w(t)} \sum_t w(t)\tilde{u}_{y,i}(t)e^{-2\pi i f t}, \tag{33}$$

The factor of 2 comes from the fact that when averaging out the Hann weights we get a value of $1/2$ so to restore the actual complex amplitudes we divide by $1/2$, or multiply by 2. The Hann weight is defined as,

$$w[n] = \frac{1}{2}\left(1 - \cos\left(\frac{2\pi n}{N-1}\right)\right) \tag{34}$$

where $N$ simply corresponds to the number of frames and $n$ to the current frame being evaluated.

With the complex amplitudes for some frequency, for both x and y, in place we can effectively find the complex amplitudes, or spectral powers in x and y directions, for some frequency. If this "test frequency" $f$ is in the harmonics of the motion being tested, the Fourier transform will have a non-zero complex amplitude in the respective direction.

To get a single metric for the whole grid, we can define the actual spectral power as,

$$P(f) = \frac{1}{N_{dots}} \sum_i^{N_{dots}} \left[|C_{x,i}(f)|^2 + |C_{y,i}(f)|^2\right] \tag{35}$$

This is the average of the spectral power for each individual dot across the whole grid, for some frequency. Thus, the spectral power is simply a measure of the complex amplitudes for some frequency, where we combine both $P_x$ and $P_y$ , across the whole dot grid.

If this value is high, then that means that $f$ is present in the motion of the dots, if not then the frequency does not match the behaviour.

With this in our hands we can use Equation (35) to find the relevant frequencies in our video. We simply choose a suitable range of frequencies to test, find the spectral power over the dot-grid for each frequency and then plot them.

In Figure 7 we have plotted the $P(f)$ for the whole spectrum, but as we can see only a few frequencies actually have significant signatures. This run used 80% concentration of glycerol and a 15 Hz nominal driving frequency.

For a higher driving frequency, as in Figure 8, we can see that the relevant spectral powers/peaks change position in the spectrum, as expected.

One important note is about the fact that this method assumes that the oscillatory motion of the dots will match with the oscillatory motion of the wave. This is a valid worry but there is justification for this.

If one considers the slope of the wave, that bends light, and that oscillates with the frequency we want to measure, then the frequency of the apparent dot motion due to refraction will match with the frequency of oscillation of the slope. Consequently, in the small-slope regime where the apparent dot displacement is related to the surface gradient through refraction, the dominant frequency of the apparent dot motion should match the dominant frequency of the surface slope itself. For a more in-depth analysis, see Moisy et al. [13] and also of particular interest see Li et al. [22], for a single-camera formulation relating apparent marker displacement to surface height and surface gradients.

## B.4 Onset $\Gamma$ estimation

To extract estimates of onset acceleration $\Gamma_z$ we must follow the same process delineated in the previous sections, however now the videos we are analysing are run-up videos, as described in Section 3. The main idea will be to extract the spectral power Equation (35), particularly for half-harmonic frequencies, but now this will be a function of time, since the videos do not have a stable amplitude produced by the shaker, with stable waves, but rather a varying amplitude. The core theoretical observation is that at onset the waves overcome the damping of the fluid and reach instability, this happens first at half-driving frequency, and this instability leads to an exponential increase of the spectral power of the half-harmonic frequency, as the frequency becomes more and more prominent, until the wave stabilises in that state. Thus, by analysing when the exponential increase starts we can determine the absolute time of onset, which can finally be cross-referenced with the accelerometer's $\Gamma$ values.

The process of Section B.2 as well as Section B.3 remains the same, and from these methods we can extract the displacements $(\Delta x(t), \Delta y(t))_i$ Equation (26) for each dot indexed on the grid by $i$, as well as the spectral power $P(f,t)$ Equation (35), over time. However, what does fundamentally change is how we extract the data from the accelerometer, delineated in Section B.1. Different from before, where we could simply consider the whole window of the stable video, where amplitude was constant, and extract the envelope of it, now, however, we must consider a small window around the value of $t$, and then find the envelope of that sample, which allows us to get the amplitude, namely $\Gamma$.

Using this method we can graph the root of the spectral power $\sqrt{P_{f/2}(t)}$ over time (we graph the root because $P(f)$ has $\text{px}^2$ units, so by taking the root we use px units which makes the function look more continuous, but fundamentally the relation stays the same.), as well as the accelerometer's gamma values over time $\Gamma(t)$ in the same plot, as can be seen in Figure 28.

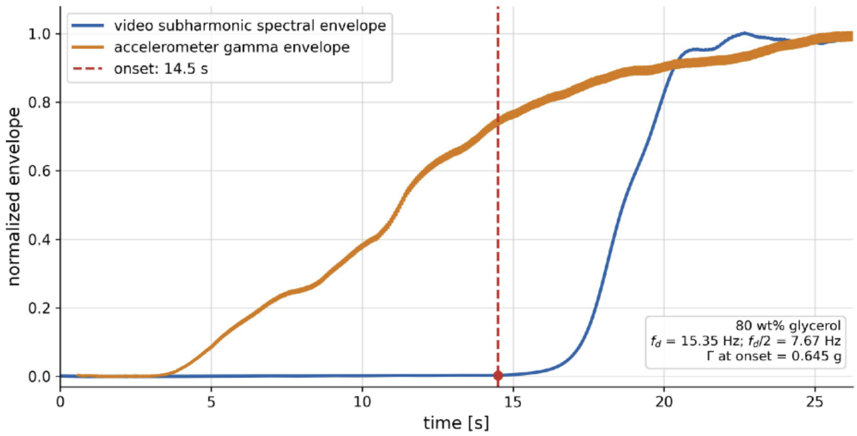


Figure 28: Graph of the accelerometer's gamma values over time, as well as the root of spectral power of the half-harmonic frequency. Both curves are plotted in normalised coordinates, such that comparison can be actually viable.

As we can see there is a clear exponential increase in the spectral power, which is expected given that after onset the half-harmonic frequency band overcomes damping. However, it is hard to see exactly the moment when the spectral power becomes exponential, so we graph it on a logarithmic scale, as can be seen in Figure 29.

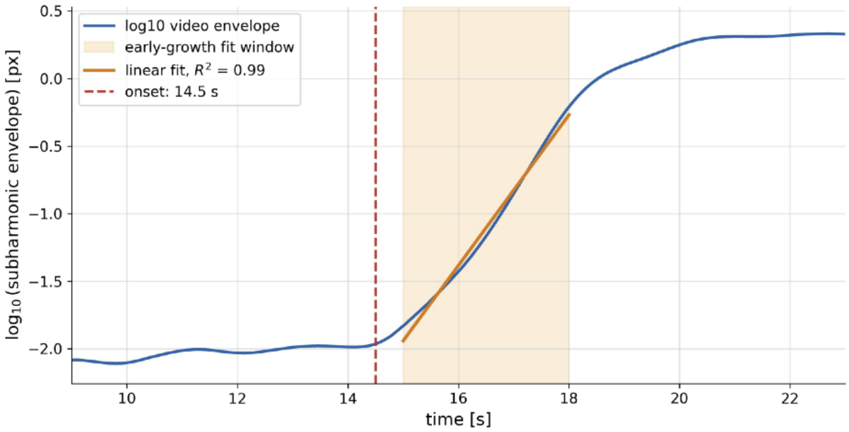


Figure 29: Graph of the root of half-harmonic spectral power, on a logarithmic scale. Window of linearity graphed for visual purposes as well as a simple linear fit over the window. Onset value chosen at the start of linearity.

Now it becomes clearer to see the moment when the log-curve becomes very linear - this is the moment when exponential increase becomes truly relevant and thus the moment of onset. Finally, we use this extracted time value $t_{onset}$ and then with the accelerometer's data we obtain,

$$\Gamma_z = \Gamma(t_{onset}) \tag{36}$$

## B.5 FSSS reconstruction

FSSS, or Free-surface synthetic schlieren, is a method that is often used in the context of reconstructing fluid interfaces. It consists of tracing the trajectories of light rays, as they are refracted by the deformed fluid surface, and from these refracted trajectories one can relate the apparent dot motion observed by the camera to the gradients of the surface itself. Then, by solving a least-squares problem it is possible to integrate over this extracted gradient field to obtain the actual height $\zeta(x, y, t)$ of the waves.

For a starting point in the study of this method, particularly regarding Faraday waves, one may consult Pedersen et al. [2], and for a more in-depth overview Moisy et al. [13] as well as for particularly free-surface interfaces Li et al. [22].

Since this is quite a complicated section, with multiple intermediate quantities, it is best to define exactly what we want to extract from the start.

First, the goal is to find a matrix **B** that satisfies,

$$\nabla\zeta(x, y) = (\partial_x\zeta, \partial_y\zeta) = \mathbf{B}\Delta\vec{r}_{mm} \tag{37}$$

where, in this case, $\zeta$ need not be the wave we are reconstructing, but just a valid height map with known refraction and analytical equation (this is the whole idea of FSSS, we are constructing "synthetic" and known surfaces and then using these synthetic surfaces to find the relationship between dot displacement and slope of the deformed fluid.), and $\Delta\vec{r}_{mm}$ is the displacement of the dots in the plane of the physical dot-grid.

Thus, we seek to obtain a matrix that relates the surface gradient of a height map $\zeta(x, y, t)$ with the apparent dot motion, due to the wave deforming the surface of the fluid, and the refracted light rays changing the apparent position of the dot, as seen by the camera.

For this we need a large selection of valid combinations of $(\nabla\zeta, \Delta\vec{r}_{mm})$ which then allows us to solve Equation (37) as a least-squares problem.

After we have **B**, we can effectively construct a gradient field $\nabla\zeta(x, y, t)$ for each surface instance of the video, by directly using the known dot displacements $\Delta\vec{r}_{mm}(t)$.

From here, we can integrate over this gradient field to find the actual height map $\zeta(x, y, t)$ over time (for each frame).

Then, we can use this height map to do a Fourier transform which allows us to extract the dominant wavelength of the surface, and then from here we calculate the wavenumber $k$ that entered the instability state, which led to the Faraday waves.

### B.5.1 The FSSS transformation matrix B

We can use the same methods as introduced in Section B.2 to obtain the positions of the dots, in pixels, $(x_{dot}, y_{dot})$, this represents the positions of the dots as viewed by the camera, for clarity of nomenclature let us define the position of the dots as seen by the camera (in pixels) as $(u, v)$.

Then from here, we can effectively build the dot-grid coordinate system, by assuming that the dots are at $d = 1$ mm separation, and thus the plane of the dot grid can be defined as,

$$(X, Y, Z) = (x_{grid}, y_{grid}, 0) = (id, jd, 0) \quad i, j \in \mathbb{N} \tag{38}$$

where naturally the indices $i, j$ are natural numbers that run from 0 to some value, depending on the grid size defined by the ROI. (This assumes the convention that one of the corner dots is defined as $(0, 0)$)

Again, for clarity, $(x_{grid}, y_{grid})$ represent the physical positions, in the physical coordinate system of the dot-grid. This is entirely different from the defined $(u, v)$ since those are the positions of the dots in the camera reference frame.

With this at hand we can find the camera pose using *cv2.solvePnP()*, which gives us the position of the camera relative to the coordinate system of the dot grid, let us call this vector **C**.

Now, using the flat liquid reference video, as defined in Section 3, we can find the dot positions $(u_{grid}, v_{grid})$, in this image with normal tracking as defined in Section B.2 (be careful with the reference frame, these dots are in the camera reference frame).

Finally, using the position of all the dots, as defined by our dot-grid coordinate system $(x_{grid}, y_{grid})$ (in SI units) as well as the dot positions in the frame of the camera $(u_{grid}, v_{grid})$ (in pixel units) we fit a homography matrix **H** using *cv2.findHomography()*, which gives us a transformation between $(u, v) \rightarrow (x_{mm}, y_{mm})$ (pixels $\rightarrow$ mm). This transformation allows us to take the apparent dot motion, as seen from the camera, and transform it into the physical position of the dots.

Next, with the dot displacements written in SI units, as well as the entire optical stack from the setup (for a basic visual of the ray tracing through an optical stack, read Pedersen et al [2]), namely,

acrylic plate: 3 mm, $n = 1.49$;

polystyrene bottom: 2 mm, $n = 1.59$;

liquid depth: Calculated from Section B.1;

liquid refractive index: Interpolated as described in Section B.1;

air: $n = 1$;

We can use the main computational concept, as described in [13] and [22], to create synthetic surfaces with known gradients

$$\zeta(x, y) = A\cos(ks + \phi) \Rightarrow \nabla\zeta = -Ak\sin(ks + \phi)\nabla s \tag{39}$$

where $s$ is $x, y$ or some diagonal direction in the dot-grid plane.

We start by choosing a synthetic surface and a dot position, and then the fundamental conceptual idea is very simple, we ask "for this known synthetic surface and for this known dot position in the grid, what is the point $Q(q_x, q_y, \zeta(q_x, q_y))$ in the surface, that the light ray must pass through, such that $\vec{r}_{hit} - \vec{r}_{dot,mm}$ gets minimised?", where $\vec{r}_{hit}$ is the point where the light ray from the camera reaches the plane of the dot-grid after it refracts through the point $Q$ in the synthetic surface.

This yields a least-squares problem where we want to minimise this difference and effectively find the point $Q$ on the surface, where the camera light ray gets refracted to a dot in the physical dot-grid.

It is important to remember what the point $Q$ is: If we consider the camera emitting a light ray from its position $\mathbf{C}$, and this light ray interacts with the deformed surface at point $Q$, and the refracted light ray, through the optical stack, maps to a known dot position, then we know that this optical configuration means the coordinates of point $Q$ will be the coordinates of the dot as seen by the camera, there is no refraction happening anymore (other than air), and thus $Q$ will be the position of the dot in the camera reference frame.

After point $Q$ is found we project its coordinates into its pixel coordinates, using the found $\mathbf{C}$ for the camera as well as the camera matrix $\mathbf{K}$ - this effectively gives us the position of $Q$ in the camera reference, and finally we use the homography matrix $\mathbf{H}$ to convert this pixel point into SI units.

It is important to pause and understand what we just obtained. Since $Q$ is the point that is seen by the camera where the refraction of the rays coincides with the position of the dot we are considering in the dot-grid, then converting $Q$ into the camera frame and then using the homography to convert it to SI units, we now have the position of the dot in the dot-grid after it is refracted due to the surface, let us call this $\vec{r}_{obj}$ - so simply speaking, this is the physical position of the dot after refraction.

The same process is conducted on a flat surface with the calculated fluid height, assuming the fluid is perfectly horizontal, which then leads to the point $Q_{flat}$, and then we convert this point

$Q$ with the same process above - which leads us to obtain the physical position of the dot, after refraction due to the flat liquid, which is not deformed. Basically our baseline grid.

This allows us to define $\Delta\vec{r}_{obj} = \vec{r}_{obj} - \vec{r}_{obj,flat}$, which is the physical displacement of the dot due to refraction. Furthermore, with the $Q_i$ known for dot $i$, we can simply find the gradient of the surface at that point with $\nabla\zeta(Q_i)$ - Consequently, we have just found a valid, physical, combination of the surface slope $\nabla\zeta$ and the displacement caused by such slope $\Delta\vec{r}_{obj,mm}$.

Finally, with the recorded dot displacements as well as the known surface gradients, for a large number of successful combinations of $(\Delta\vec{r}_{obj}, \nabla\zeta(Q))_i$ (for many dots), we solve for the FSSS transformation matrix $\mathbf{B}$ from,

$$\nabla\zeta(x, y) = (\partial_x\zeta, \partial_y\zeta) = \mathbf{B}\Delta\vec{r}_{obj,mm} \tag{40}$$

This gives us a mapping between the dot displacements and surface gradients, which allows us to effectively define a gradient field $\nabla\zeta(x, y)$, based on the displacements of the dots, over the ROI.

#### B.5.2 The $\zeta(x, y, t)$ surface height map

With the FSSS transformation matrix $\mathbf{B}$, we can now obtain the gradient field for each frame of a video. For every video, we track the dot positions $(u(t), v(t))_i$ per frame and then using the homography matrix $\mathbf{H}$ we obtain the physical displacements of each dot $(\Delta x_{mm}, \Delta y_{mm})_i$.

Using the transformation matrix,

$$\begin{pmatrix} p_i \\ q_i \end{pmatrix} = \begin{pmatrix} \partial_{x,i} \\ \partial_{y,i} \end{pmatrix} = \mathbf{B} \begin{pmatrix} \Delta x_i \\ \Delta y_i \end{pmatrix} \tag{41}$$

This allows us to obtain the slopes of the fluid surface, for each displacement $(\Delta x(t), \Delta y(t))_i$.

With this gradient field we can simply solve this as a 2D least-squares problem,

$$\min\left(\sum_{\zeta} \left[(D_x\zeta - p)^2 + (D_y\zeta - q)^2\right]\right) \tag{42}$$

where $D_x$, $D_y$ are finite difference operators between neighbouring points. One important note is that computationally we are structuring our $\zeta$ as a linear problem $\mathbf{A}\vec{z} \approx \vec{b}$, where $\vec{z}$ is the vector with all height values we want to obtain, $\mathbf{A}$ is the matrix that computes differences between neighbouring height values and $\vec{b}$ contains the measured slopes times grid spacing.

So fundamentally we are solving many equations of the form,

$$\zeta_{i+1,j} - \zeta_{i,j} \approx p_{i+1/2,j}\Delta x \qquad (x - direction) \tag{43}$$

$$\zeta_{i,j+1} - \zeta_{i,j} \approx q_{i,j+1/2}\Delta y \qquad (y - direction) \tag{44}$$

where the half index comes from interpolation of the measured slope values between adjacent dots.

At last, we have obtained the actual height map for the surface, for each frame of the video.

### B.5.3 Spatial Fourier analysis and wavenumber

With our height map we can perform the same process as was done in Pedersen et al [2], taking directly the formula they used,

$$A_{\mathrm{FT}}(k_x, k_y) = \frac{1}{MN} \sum_{m=0}^{M-1} \sum_{n=0}^{N-1} A(x_n, y_m) e^{-ik_x x_n} e^{-ik_y y_m} \tag{45}$$

Where $A(x, y) = \zeta(x, y)$ for some frame.

We can then multiply this by the Hann window Equation (34) as well, otherwise we would get spectral leakage due to lack of spatial periodicity,

This Fourier transform gives us a 2D Fourier Amplitude map $A_{FT}(k_x, k_y)$ (similar to $\sqrt{P(f)}$), but now for spatial correlation with wavenumbers in x and y directions, namely $k_x, k_y$, instead of a frequency $f$. We can convert each wavenumber to its particular wavelength $\lambda_x, \lambda_y$, and then combine them into a scalar,

$$\frac{1}{\lambda} = \sqrt{\frac{1}{\lambda_x^2} + \frac{1}{\lambda_y^2}} \tag{46}$$

This fundamentally gives a spectrum based on the present wavelength $A(\lambda)$. Finally, we simply extract the dominant wavelength peak, which is the wavelength with the highest spatial spectral power $A(\lambda)$, and then convert it to the dominant wavenumber $k$, which should match with the wavenumber that entered instability which led to the Faraday standing waves.

# C GitHub Repository

All code developed for this experiment, from the numerical methods defined in the Section 1, as well as a script for calculating the relevant quantities regarding fluid properties and the entire pipeline for frequency analysis, onset estimation and spatial analysis from FSSS can be found in this public GitHub repository:

Github Repository (https://github.com/Liaust/faraday-waves-toolkit)

It contains not only the code but, via the comments written in each script, one can understand much that was not referenced in the methodology described in this paper.